UNIVERSITY OF COPENHAGEN
FACULTY OF SCIENCE

MSc in Physics

Tidal Disruption Events as Sources of High-Energy Neutrinos

Manuel Goimil García

Supervised by Markus Ahlers and Enrico Peretti

May 2023

Manuel Goimil García

Tidal Disruption Events as Sources of High-Energy Neutrinos

MSc in Physics, May 2023

Supervisors: Markus Ahlers and Enrico Peretti

University of Copenhagen

Faculty of Science

Niels Bohr Institute

Blegdamsvej 17

2200 Copenhagen N

I have done a bad thing. I have postulated a particle that can not be detected.

Wolfgang Pauli

Abstract

This thesis presents a time-dependent model of neutrino production in three Tidal Disruption Events (TDEs) associated with events in the IceCube Observatory: AT2019dsg, AT2019fdr and AT2019aalc. Comparisons between typical time scales of diffusive shock acceleration and energy losses are used to place a high-energy cut-off on an initial power-law spectrum of cosmic rays, whose time evolution is determined numerically with a linear Fokker-Planck equation dominated by continuous (photo)hadronic and radiative cooling. Secondary neutrino, γ-ray and electron fluxes are then calculated by folding the resulting spectrum with analytic estimates of their production cross sections. The electromagnetic spectrum of primary electrons and secondary products of cosmic-ray interactions is compared with Fermi-LAT upper bounds from the non-detection of γ-rays, and features that could serve as evidence of (photo)hadronic interactions in TDEs are discussed. Likewise, the neutrino flux is integrated over the duration of the events to compare the total fluence with IceCube differential limits.

Acknowledgements

While working on this thesis, I thought often of former professor Ricardo Vázquez from the University of Santiago de Compostela, who passed away last winter. His talks about cosmic rays introduced me to multi-messenger astronomy when I was in high-school and motivated me to study Physics. I hope to achieve his clarity and depth of knowledge one day, and dedicate this work to him.

On a happier note, I feel very lucky to have enjoyed the guidance of my current associates at the Niels Bohr Institute. First and foremost, thanks to Enrico Peretti and Markus Ahlers for their dedication, and for their enduring patience as I struggled with my own code. Thanks as well to the PhD and post-doc staff at the Institute for their enthusiasm and for valuable talks, both in the Academy and at Søernes.

Finally, I want to include a mention of the dear personal relations I have neglected during my writing spree. In particular, I am very grateful to Rasmus and Caro for their continued encouragement and affection; to Emil, for many, many, many (but not too many) shared coffees; and most especially to Liv, who has been my biggest support these last months. They, along with many others, have influenced this work too.

Copenhagen, May 2023

Contents

1 Introduction **3**

2 Theoretical background **5**

2.1 Tidal disruption in the impulse approximation 5

2.1.1 Newtonian condition for tidal disruption 5

2.1.2 Fallback and circularization 7

2.1.3 Dissipation of angular momentum in the super-Eddington regime 9

2.2 Diffusive shock acceleration 11

2.2.1 Heuristic derivation of the energy gain 11

2.2.2 Acceleration time scale 13

2.3 Cooling mechanisms in astrophysical environments 14

2.3.1 (Photo)Hadronic interactions I: meson production 14

2.3.2 (Photo)Hadronic interactions II: Bethe-Heitler pair production 16

2.3.3 Inverse Compton scattering 17

2.3.4 Radiative cooling I: synchrotron emission 18

2.3.5 Radiative cooling II: bremsstrahlung 19

2.4 Fokker-Planck equation 20

3 Model of high-energy emission from Tidal Disruption Events **23**

3.1 Radiation zone and scattering backgrounds 23

3.1.1 Definition and size of the radiation zone 23

3.1.2 Normalization of the scattering backgrounds 25

3.2 Injection of non-thermal particles 26

3.2.1 Assumption on the injection spectrum 26

3.2.2 Estimation of the high-energy cut-off 27

3.2.3 Normalization of the primary injection spectra 28

3.3 Numerical treatment of the Fokker-Planck equation and calculation of secondary spectra 28

4 Multi-wavelength and neutrino emission from Tidal Disruption Events **31**
4.1 High-energy cut-off in the injection spectra 31
4.1.1 Comparison of acceleration and (photo)hadronic cooling time scales 31
4.1.2 Electron acceleration and efficiency of radiative losses . 35
4.2 Proton and electron spectra 36
4.2.1 Proton spectrum 36
4.2.2 Electron spectrum 38
4.3 Multi-wavelength electromagnetic spectra of Tidal Disruption Events 42
4.3.1 Evidence of (photo)hadronic interactions in the infrared to X-ray range 42
4.3.2 γ-ray opacity and absorption in the extragalactic medium 46
4.4 Neutrino fluences on Earth 50

5 Conclusions and outlook **53**

A Technical implementation of cooling mechanisms **55**
A.1 Bethe-Heitler cross section 55
A.2 Synchrotron radiation in matter: plasma frequency and Razin-Tsytovich effect 56

B Normalization and time evolution of target backgrounds **59**
B.1 Fiducial parameters 59
B.2 Limitations on the analytic study of the fallback rate 60

C Consistency tests **63**
C.1 Self-consistency of the linear approximation 63
C.2 Comparison with existing literature 64

Bibliography **67**

1 Introduction

Tidal Disruption Events (TDEs) are transient sources of high-energy particles, namely $\mathcal{O}(100)$ d- to $\mathcal{O}(1)$ yr-long electromagnetic flares that occur when a star gets torn apart by the gravitational pull of a much more massive object [1]. Signals from tens of galactic nuclei, mainly in the optical-ultraviolet (OUV), but also up to X-ray and down to radio energies, have been attributed to the tidal disruption of stars by black holes of $10^6 - 10^8$ solar masses (e.g. [2–4]).

Although the existence of these Super-Massive Black Holes (SMBHs) was postulated to explain 10^7 yr-long multi-wavelength signals from so-called active galactic nuclei, their presence is expected at the center of most galaxies. Current cosmological models strongly favour the view that the latter coalesced around these objects, which had originated previously due to initial inhomogeneities in the density profile of the Universe [5, 6]. TDEs thus offer the opportunity to study the early history of structure formation by probing the characteristics of SMBHs in the larger population of otherwise quiescent or weakly-emitting galactic nuclei [7].

However, such an approach requires a robust description of how TDE emissions are powered, which is hard to obtain from observations of electromagnetic flares: observational estimates of their bolometric luminosity, time-evolution and energy distribution can be subject to large uncertainties, e.g. due to absorption along the line of sight [8]. In this context, recent efforts to develop phenomenological models of these sources (e.g. [9]) have been driven by associations between TDEs and the detection of 100 TeV neutrinos [10, 11].

Neutrino astronomy has developed rapidly over the last decades, in large part as an answer to the difficulties in detecting radiative emissions from high-energy cosmic sources [12]. These particles propagate ballistically, without significant energy losses or absorption, because they have no electric charge and only scatter in weak interactions: thus, models of time-dependent neu-

trino emissions are very accurate probes into the dynamics of astrophysical environments.

Furthermore, neutrino production is expected in connection with the acceleration of $\gtrsim$PeV protons and heavier nuclei in astrophysical environments [13, 14]. TDEs have long been proposed as sources of PeV energy Cosmic Rays (CRs) [15], i.e. high-energy protons, electrons and positrons (hereafter electrons, for short), and might be able to accelerate particles to EeV energies in jets if the disrupted star is massive enough [16]. Such ultra-high-energy CRs have already been observed on Earth, but carry no directional information on their sources because they are deflected by magnetic fields. Thus, besides its application to SMBH demographics, the study of neutrino production in TDEs could help determine the origin of some of the most energetic particles in the Universe. Research on non-jetted TDEs would also constrain the parameter space of sources of the diffuse neutrino background, an isotropic distribution of neutrinos to which such transients could contribute $\lesssim 30\%$ of the total [17].

The present thesis focuses on the latter type of TDEs, attempting to reproduce and expand on [18], which discusses several time-dependent models of neutrino emission in the three TDEs associated with IceCube alerts (AT2019dsg, AT2019fdr and AT2019aalc). Said article tries to determine what benchmark scenarios of CR interactions are consistent with the alerts and to give a prediction of the time-integrated neutrino flux in each model, using estimates of the SMBH and disrupted star masses from infrared (IR), OUV and X-ray surveys. The aim of this work has been to calculate the neutrino fluences from these same sources, improving upon the results in the literature by determining the maximum CR energy self-consistently, and complimenting the calculation with an estimate of the electromagnetic spectrum emitted by CRs and products of their interactions.

The thesis is structured as follows: Chapter 2 presents the theoretical background of tidal disruption, particle interactions around the SMBH, and the transport equation in momentum space; Chapter 3 discusses the numerical model used to calculate the fluences; Chapter 4 shows and interprets the neutrino fluxes and electromagnetic spectra obtained in this framework, and Chapter 5 offers a summary and an outlook on future work.

Theoretical background

2

This chapter presents the main physical processes which lead to the emission of electromagnetic radiation and high-energy neutrinos in TDEs. In summary, part of the energy dissipated in the accretion of stellar matter onto an SMBH results in the acceleration of non-thermal particles. Astronomical messengers are produced when said particles cool in interactions with low-energy background radiation and gas.

In Section 2.1, a model of TDEs is discussed, and used to obtain an analytic estimate of the time scale on which matter falls towards the SMBH. In Section 2.2, diffusive shock acceleration (DSA) is proposed as the main particle acceleration mechanism in TDEs, and its time scale and resulting spectrum are derived. In Section 2.3, the time scales of the energy losses that compete with acceleration are presented. Finally, the transport equation of non-thermal particles in momentum space is derived in Section 2.4.

2.1 Tidal disruption in the impulse approximation

2.1.1 Newtonian condition for tidal disruption

Two test particles moving along trajectories $\mathbf{x}_1(t)$ and $\mathbf{x}_2(t) = \mathbf{x}_1(t) + \mathbf{n}(t)$ in a position-dependent potential $V(\mathbf{r})$ will accelerate relative to each other. Subtracting the equations of motion of both particles in the limit $\mathbf{x}_2 \to \mathbf{x}_1$ shows that the time-dependence of the separation vector $\mathbf{n}(t)$ is proportional to the matrix elements of the Hessian, $H_{ji} = -\partial^2 V/(\partial x_j \partial x_i)$ [19]:

$$\frac{\partial^2 n_i}{\partial t^2} + \frac{\partial^2 V}{\partial x_j \partial x^i} n_j = 0 \tag{2.1}$$

This result, which is generally called differential acceleration, can be applied to simplified analyses of tidal disruption [20]. The infinitesimally-close test particles then correspond to mass elements in a continuous mass distribution, namely a star, and $V(\mathbf{r})$ is the Newtonian potential generated by an SMBH with mass $M_\bullet$, i.e. $V(r) = -GM_\bullet/r$. In polar coordinates (Figure 2.1), the corresponding equations of motion are:

$$\frac{\partial^2 n_\mathrm{r}}{\partial t^2} = \frac{2GM_\bullet}{r^3} n_\mathrm{r} \qquad \frac{\partial^2 n_\varphi}{\partial t^2} = -\frac{GM_\bullet}{r^3} n_\varphi \qquad \frac{\partial^2 n_\mathrm{z}}{\partial t^2} = -\frac{GM_\bullet}{r^3} n_\mathrm{z}, \tag{2.2}$$

so the star gets stretched along the radial axis ($H_\mathrm{rr} > 0$) and compressed along the orthogonal ones ($H_{\varphi\varphi} = H_\mathrm{zz} < 0$).

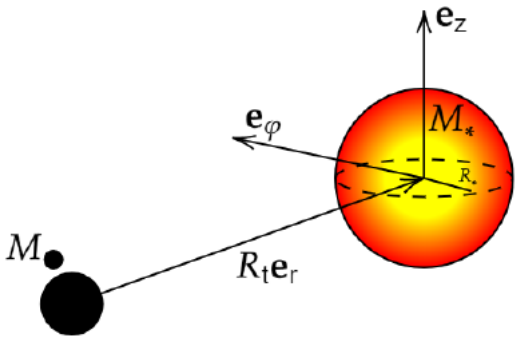

Figure 2.1.: Coordinate system in the Newtonian treatment of tidal disruption.

The impulse approximation assumes that the star resists deformation until its center of mass gets close enough to the SMBH for $H_\mathrm{rr} n_\mathrm{r}$ to overcome the stellar gravity. At that point, all internal forces become negligible and the disrupted mass elements are transported along ballistic orbits in the external potential $V(r)$ [21]. In short, the star remains in equilibrium until it is instantly destroyed. For a spherically symmetric distribution with size $R_* \simeq n_r$, the tidal radius R_t at which a star with mass M_* will be tidally disrupted is therefore:

$$R_\mathrm{t} \sim R_* \left(\frac{M_\bullet}{M_*}\right)^{1/3} \sim 1.5 \times 10^{13}\ \mathrm{cm} \left(\frac{R_*}{R_\odot}\right) \left(\frac{M_\bullet}{10^7 M_\odot}\right)^{1/3} \left(\frac{M_*}{M_\odot}\right)^{-1/3}. \tag{2.3}$$

The Newtonian treatment is relatively accurate in the region of parameter space where R_t is much larger than the size of the event horizon, which

in Schwarzschild space-time is $R_\mathrm{s} = 2GM_\bullet/c^2$. The first few Schwarzschild corrections to the equations of motion are absorbed into the cubic root in (2.3) [19, 22], while effects induced by black-hole spin fall off quickly with distance and may be neglected in the region $r \gtrsim 5R_\mathrm{s}$ [23]. However, if the SMBH is sufficiently massive, the whole star may fall into it. This places an upper bound on $M_\bullet$, often referred to as the Hills mass (e.g. [24]):

$$M_{\bullet,\mathrm{H}} \sim 10^8 M_\odot \left(\frac{R_*}{R_\odot}\right)^{3/2} \left(\frac{M_*}{M_\odot}\right)^{-1/2}, \tag{2.4}$$

where $M_\odot$ ($R_\odot$) is the mass (radius) of the Sun.

2.1.2 Fallback and circularization

High-energy emissions from TDEs are powered by energy losses in the fraction of stellar matter that becomes bound to the SMBH during disruption. Said energy losses are mainly caused by the circularization of stellar debris into an accretion disc and to viscous drag within the disc itself. Signals from TDEs are expected to follow the rate at which disrupted material falls into the SMBH ($\dot{M}$) as a result of these two processes.

After disruption, bound stellar debris forms an elongated stream that initially travels along a highly eccentric trajectory. Circularization takes place over a time scale of several orbital periods due to the apsidal precession of this orbit in the strong gravity of the SMBH, which makes the stream collide inellastically with itself [25, 26]. In a post-Newtonian framework, precession can be modelled as an instantaneous shift in the trajectory that occurs upon return to the orbital pericenter, so self-intersection is expected when the most bound region of the stream, which has already completed one revolution around the SMBH, crosses with the region that is still falling back towards it (Figure 2.2). For $M_\bullet \gtrsim 10^7 M_\bullet$, the predicted collision radius is much smaller than the orbital apocenter [27], so the intersection rate is dominated by the the fallback rate of the most bound debris. Assuming that disruption occurs close to the pericenter, the circularization rate at time t is therefore proportional to the amount of matter with orbital period $T \sim t$:

$$\dot{M}_\mathrm{circ}(t) \sim \dot{M}_\mathrm{fallback}(T = t) \equiv \left.\frac{\partial M_*}{\partial T}\right|_{T=t}. \tag{2.5}$$

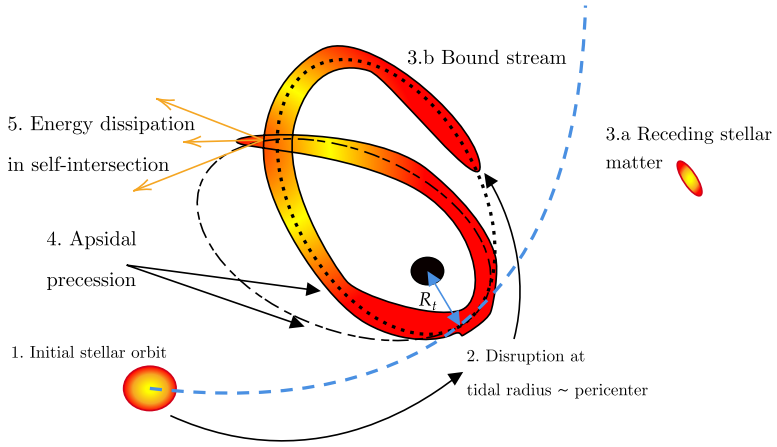

Figure 2.2.: Disruption and fallback along an elliptic Keplerian orbit. Relativistic corrections to the gravity of the SMBH lead to apsidal precession and self-intersection of the bound stream upon its return to pericenter.

Internal forces in the stream and interactions with the unbound stellar debris are considered negligible, and in the impulse approximation there are no deformations like (2.2) that could lead to velocity perturbations inside the star [28]. Thus, the trajectory of each mass element is solely determined by its specific energy in the external potential $V(r)$, i.e. $T = T(\epsilon_g)$:

$$|\epsilon_g(r)| = \frac{GM_\bullet}{r}. \tag{2.6}$$

In these conditions, the orbital period can be estimated using Kepler's third law, which can be deduced by stating that the Newtonian gravity of the SMBH acts as a centripetal force:

$$T(\epsilon_g) \simeq \frac{\pi}{\sqrt{2}} GM_\bullet |\epsilon_g|^{-3/2}. \tag{2.7}$$

This result can be used to determine the time evolution of the circularization rate by applying the chain rule to (2.5):

$$\dot{M}_{\text{circ}} \sim \frac{\partial M_*}{\partial |\epsilon_g|} \left| \frac{\partial \epsilon_g}{\partial T} \right|. \tag{2.8}$$

Under the current assumptions, $\partial M_*/\partial|\epsilon_g|$ is flat and time-independent: its center lies at the orbital energy of the stellar center of mass and its width

$(2\Delta\epsilon_{\rm g})$ is given by the spatial spread of the star at the moment of disruption. For a homogeneous, spherically symmetric star on a nearly-parabolic orbit:

$$\frac{\partial M_*}{\partial|\epsilon_{\rm g}|} \sim \begin{cases} \dfrac{M_*}{2\Delta\epsilon_{\rm g}}, & (|\epsilon_{\rm g}| < \Delta\epsilon_{\rm g}) \\ 0, & \text{otherwise} \end{cases} \quad , \quad \Delta\epsilon_{\rm g} \sim \frac{GM_\bullet}{R_{\rm t}}\frac{R_*}{R_{\rm t}}. \tag{2.9}$$

The circularization rate $\dot{M}_{\rm circ}$ may then be written in terms of an effective luminosity $L_{\rm fallback} = \dot{M}_{\rm fallback}c^2$:

$$L_{\rm fallback}(t) \sim 10^{47}\ {\rm erg\ s^{-1}} \left(\frac{M_\bullet}{10^7 M_\odot}\right)^{1/3} \left(\frac{M_*}{M_\odot}\right)^{1/3} \left(\frac{R_*}{R_\odot}\right) \left(\frac{t}{100\ {\rm d}}\right)^{-5/3}, \tag{2.10}$$

where T runs from the period of the orbit with specific energy $\epsilon_{\rm g} = -\Delta\epsilon_{\rm g}$ to infinity.

Hydrostatic equilibrium between the gravitational pull of a mass $M_\bullet$ and its radiation pressure is achieved when its luminosity reaches the Eddington level:

$$L_{\rm edd} \simeq 1.26 \times 10^{45}\ {\rm erg\ s^{-1}} \left(\frac{M_\bullet}{10^7 M_\odot}\right). \tag{2.11}$$

When $L > L_{\rm edd}$, outward forces drive matter away from the central body, and viceversa. Equation (2.10) shows that for $M_\bullet \sim 10^7 M_\odot$ and $M_* \sim M_\odot$ the fallback rate can be expected to be super-Eddington ($L_{\rm fallback} > L_{\rm edd}$) during a period of a few years, so emissions from TDEs are likely to be accompanied by outflows of stellar material from the disc.

2.1.3 Dissipation of angular momentum in the super-Eddington regime

After circularization, stellar debris accretes onto the SMBH due to dissipation of angular momentum in the disc. The viscous-drag time scale is given by [29, 30]:

$$t_{\rm vis}(r) \sim \frac{r^2}{\nu} \sim \frac{15}{2\pi}\left(\frac{0.1}{\alpha}\right)\left(\frac{r}{H}\right)^2 T_{\rm c}(r), \tag{2.12}$$

where $T_{\rm c}(r)$ is the period of a circular Keplerian orbit at a distance r from the SMBH, $0 < \alpha < 1$ is a stress-to-pressure ratio that models the effect of turbulence on the viscosity ν, and H is the height scale of the disc.

The latter is expected to be of order $H \sim r$, because the efficiency of radiative cooling in the bound stream is low. Equation (2.10) implies that the duration of the fallback is much shorter than typical photon diffusion time scales [28], so most of the potential-energy loss caused by each collision must be converted into thermal pressure. Work on the most weakly-bound debris makes the stream expand and could also drive the emission of plasma outflows in each collision [28, 31].

Since the disc is geometrically thick, instabilities in the magnetic field of the plasma may lead to high enough α for matter to accrete on the time scale of its orbital period, $t_{\text{vis}}(r) \sim \mathcal{O}(1)T_{\text{c}}(r)$ [25, 32]. Conservation of angular momentum in self-intersection collisions may be used to show that stellar debris circularizes at a radius $r_{\text{c}} \sim 2R_{\text{t}}$ [25], which for $M_\bullet \sim 10^7 M_\odot$ and a solar-type star yields $t_{\text{vis}}(r_{\text{c}}) \sim T_{\text{c}} \sim 10^4$ s. In comparison, (2.7) and (2.9) imply that the first orbital period of the most bound debris ($\epsilon_{\text{g}} = -\Delta\epsilon_{\text{g}}$) from a star approaching on a parabolic orbit is:

$$T_{\text{min}} \sim 3.1 \times 10^6 \text{ s} \left(\frac{M_\bullet}{10^6 M_\odot}\right)^{1/2} \left(\frac{M_*}{M_\odot}\right)^{-1} \left(\frac{R_*}{R_\odot}\right)^{3/2}. \tag{2.13}$$

Hence, the accretion rate is dominated by the first return to pericenter:

$$\dot{M}(t)c^2 \sim L_{\text{fallback}}(t). \tag{2.14}$$

This result is relevant for the study of TDEs because it provides a way to test analytic descriptions of the formation of the accretion disc against observational data. A fraction of $\dot{M}(t)c^2$ radiated away from the SMBH in the form of e.g. OUV signals, whose time evolution is expected to trace the accretion rate [18]. $\dot{M}$ can thus be defined in terms of the observed bolometric luminosity $L_{\text{ouv}}(t)$ and a normalization factor $\dot{M}(0)$ at the peak of the optical emission:

$$\dot{M}(t) = \dot{M}(0)\frac{L_{\text{ouv}}(t)}{L_{\text{ouv}}(0)}. \tag{2.15}$$

Comparisons between measurements and the power-law (2.10) (e.g. [10]) thus confirm the results of several simulations, which predict that the $L_{\text{fallback}}(t) \propto t^{-5/3}$ scaling is at most reproduced asymptotically at late times (e.g. [33, 34]). This seems to suggest that the accretion rate is indeed determined by fallback, so (2.14) holds, but the physics of circularization are not well described by

Keplerian derivations, at least early on. Some difficulties in the analytic derivation of the fallback rate, mostly due to possible sources of time-dependence in the energy distribution $\partial M_*/\partial|\epsilon_g|$, are discussed in Appendix B.2.

2.2 Diffusive shock acceleration

In order for 100 TeV neutrinos to be produced in TDEs, a fraction of the accretion rate $\dot{M}(t)$ must be converted into very-high-energy primary protons. The spectral distribution of these particles and the time scale over which they are produced depend on the specific acceleration mechanism that dominates in the sources. In this work, it is assumed that CRs in TDEs result from the Diffusive Shock Acceleration (DSA) of stellar debris, which is explained below.

2.2.1 Heuristic derivation of the energy gain

Electromagnetic spectra from a wide variety of sources can be associated to energy losses from power-law distributions $n_{\text{emitter}}(E) \propto E^{-\alpha}$ with spectral index $\alpha \sim 2$. The first models of particle acceleration attempted to explain this scaling by considering repeated head-on collisions of the primaries with non-relativistic magnetic clouds [35]. Hereafter, $\mathbf{U}$, Γ and $p = (E, \mathbf{p})$ are the velocity of the cloud, its Lorentz factor, and the initial 4-momentum of the particle in the observer frame.

In the cloud frame, scattering is elastic, so the energy of the particle is conserved and its momentum flips sign along the direction normal to the cloud. In the observer frame, this leads to a net energy difference ΔE that can be related to E via [36]:

$$\Delta E = E\left[\Gamma^2\left(1 + 2\frac{\mathbf{U}\cdot\mathbf{p}}{E} + \mathcal{O}(U^2/c^2)\right) - 1\right]. \tag{2.16}$$

Isotropic collisions in a gas with multiple scattering centres mean that all values of $\cos\theta \equiv \mathbf{U}\cdot\mathbf{p}/(U|\mathbf{p}|)$ are equally likely. In these scenario, averaging over $-\pi < \theta < \pi$ leads to $\langle \Delta E/E\rangle \sim \Gamma^2$: the fractional energy gain is second order in $U/c \ll 1$, because $\langle \mathbf{U}\cdot\mathbf{p}\rangle = 0$.

Acceleration becomes more efficient under the assumption that all the collisions are head-on ($\cos\theta > 0$), in which case Taylor-expanding $\Gamma^2 \sim (1 + U^2/c^2)$ for $U/c \ll 1$ and retaining only first-order terms in U/c leads to:

$$\left\langle \frac{\Delta E}{E} \right\rangle = \frac{4}{3}\frac{U}{c} \equiv \eta. \tag{2.17}$$

This outcome is expected when the particles are magnetically confined in the vicinity of collisionless shocks (e.g. [37]), which are abrupt discontinuities in the density, velocity and temperature of a medium. In astrophysical environments, they are commonly produced by supersonic perturbations of the ambient medium, and therefore propagate with velocities $\mathbf{v}_\mathrm{s}$ much faster than its speed of sound in the observer frame. If $|\mathbf{v}_\mathrm{s}| \equiv v_\mathrm{s} \ll c$, the bulk velocity of the scattering centres in the shocked (downstream) and unshocked (upstream) regions are related via $4\mathbf{v}_\mathrm{down} = \mathbf{v}_\mathrm{up} = -\mathbf{v}_\mathrm{s}$. The bulk motion of either side in the stationary frame of the other is thus given by $\mathbf{U} = \pm 3\mathbf{v}_\mathrm{s}/4$, and due to this relative sign particles traversing the discontinuity will always experience head-on collisions.

After each crossing, particles will have their velocity isotropized in the bulk and eventually travel through the discontinuity in the opposite direction, increasing their energy by a factor $1 + \eta = 1 + v_\mathrm{s}/c$ per round trip. The power-law distribution results from the finite probability v_s/c that the ones returning downstream after one cycle will be advected away from the shock, at which point they stop accelerating [35]. After k crossings, $n = (1 - v_\mathrm{s}/c)^k n_0$ particles in a cold gas with density (energy) n_0 (E_0) will reach energies $E = (1 + v_\mathrm{s}/c)^k E_0$. These expressions yield two equivalent definitions of k, from which the spectrum of particles with energy $E \geq E_0$ can be derived:

$$n(E \geq E_0) = n(E = E_0)\left(\frac{E}{E_0}\right)^{-1+\frac{\ln(1-v_\mathrm{s}/c)}{\ln(1+v_\mathrm{s}/c)}}. \tag{2.18}$$

Taylor expanding $\ln(1 + x) \sim x$ for $x \ll 1$ then leads to the universal $n(E) \propto E^{-2}$ scaling.

2.2.2 Acceleration time scale

Isotropization of particle velocity in the upstream region is required for first-order energy gain, and likely results from instabilities in the magnetic field caused by charges propagating faster than the characteristic speed in the plasma [37]. This turns particle acceleration into a non-linear phenomenon: the accelerating particles themselves generate turbulence in the gas, and interaction with this turbulence then lets them achieve higher energies.

Non-linear dynamics in general and hydrodynamic models of turbulence in particular are outside the scope of this thesis, but estimating the acceleration time scale of primary particles requires a model of the magnetic-wave power spectrum $\mathcal{P}(k)$. Fast particles initially generate eddies with some typical scale L_{max}, and the energy injected into these then cascades into to smaller currents, down to a minimum scale L_{min} where viscous dissipation becomes dominant [38]. Hence, $\mathcal{P}(k)$ is expected to have a low-wavenumber cut-off ($2\pi/L_{\text{max}}$) at the injection scale and a high-wavenumber cut-off ($2\pi/L_{\text{min}}$) at the viscous drag scale. In the intermediate so-called inertial range, turbulence is often modelled as [39]:

$$\mathcal{P}(k) \propto k^{-\gamma} \qquad \left(\frac{2\pi}{L_{\text{max}}} \leq k \leq \frac{2\pi}{L_{\text{min}}}\right), \tag{2.19}$$

The spectral index approaches $\gamma \to 1$ as the self-generated fluctuations become comparable to the unperturbed magnetic field [40]: this means that turbulence has no characteristic length because perturbations are injected at all scales. The model of particle transport in such a scenario is called Bohm diffusion: particle velocities are distributed isotropically and the mean free path is equal to the gyroradius R_{L}.

$$R_{\text{L}} = 3.3 \times 10^{12} \left(\frac{E}{\text{PeV}}\right) \left(\frac{B}{\text{G}}\right)^{-1}, \tag{2.20}$$

The DSA time scale t_{acc} may then be estimated from the characteristic diffusion coefficient of Bohm diffusion [39]:

$$D_{\text{Bohm}} = \frac{cR_{\text{L}}}{3}. \tag{2.21}$$

By definition, $t_{\text{acc}}(E) \equiv E/\dot{E}$ is η^{-1} (2.17) with $U = v_{\text{s}} \equiv v_{\text{out}}$ multiplied by the period of a round trip across the shock front, t_{diff}. The latter may be calculated using statistical kinematics: in an isotropic scenario, the flux across the shock on either direction is proportional to $c/4$, so the time required to fill a characteristic length $D_{\text{Bohm}}/(v_{\text{out}})$ upstream and $4D_{\text{Bohm}}/(v_{\text{out}})$ downstream is $t_{\text{diff}} \sim 4D_{\text{Bohm}}/(cv_{\text{out}})$ [41]. Hence:

$$t_{\text{acc}} \sim \frac{4D_{\text{Bohm}}}{v_{\text{out}}^2}. \tag{2.22}$$

The acceleration time scale (t_{acc}) can thus be estimated by comparing the Bohm diffusion coefficient to the bulk velocity of the gas (v_{out}) in the observer frame:

2.3 Cooling mechanisms in astrophysical environments

2.3.1 (Photo)Hadronic interactions I: meson production

Protons may cool via inelastic collisions with hadronic gas, which may be found in e.g. plasma outflows resulting from super-Eddington TDEs. The energy is dissipated into the production of short-lived mesons, which decay into neutrinos and photons. The largest fraction of them corresponds to charged and neutral pions (π^+, π^0):

$$\pi^+ \to \mu^+ + \nu_\mu \to (\mathrm{e}^+ \nu_{\mathrm{e}} \overline{\nu}_\mu) + \nu_\mu, \tag{2.23a}$$

$$\pi^0 \to \gamma + \gamma, \tag{2.23b}$$

although the creation and decay of η mesons also yields a minor contribution to the photon flux.

Hadronic meson production is presumably responsible for part of the γ-rays produced in astrophysical sources and it is a viable mechanism for neutrino production, given high enough target densities n_{out} [42]. From dimensional

analysis, the cooling time scale of inelastic pp collisions may be estimated as:

$$t_{\mathrm{c,pp}}(E_{\mathrm{p}}) \sim \frac{1}{K_{\mathrm{pp}} c n_{\mathrm{out}} \sigma_{\mathrm{pp}}(E_{\mathrm{p}})}, \tag{2.24}$$

where K_{pp} is the inelasticity of the collision and $\sigma_{\mathrm{pp}}(E_{\mathrm{p}})$ is the inelastic cross section at CR energy E_{p} ([13, 43], Figure 2.3):

$$\sigma_{\mathrm{pp}} = 34.3 + 1.88 \log\left(\frac{E_{\mathrm{p}}}{\mathrm{TeV}}\right) + 0.25 \log\left(\frac{E_{\mathrm{p}}}{\mathrm{TeV}}\right)^2. \tag{2.25}$$

On average, 3 pions are produced per collision, each of them carrying a fraction $E_\pi / E_p \sim 0.17$ of the primary energy, so $K_{\mathrm{pp}} \sim 0.5$ [13].

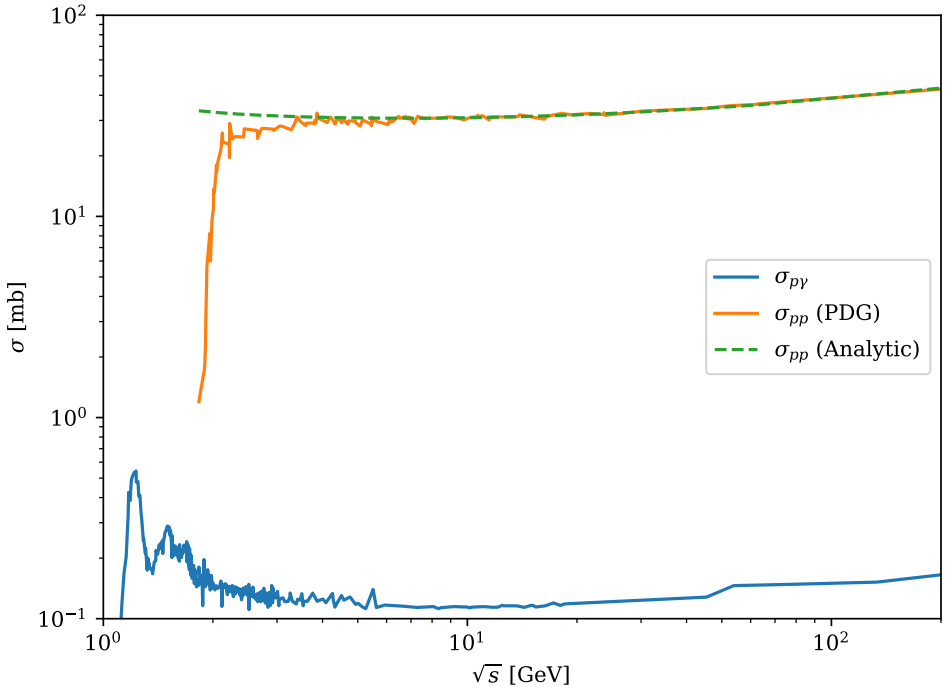

Figure 2.3.: Cross sections for pγ scattering ($\sigma_{\mathrm{p}\gamma}$; blue) and inelastic pp scattering (σ_{pp}; orange, green). The solid lines correspond to data from [43]; the dashed line is an analytic approximation given in (2.25)

Protons can also cool via meson production in collisions with low-energy radiation. The most efficient channel excites a Δ-resonance at center-of-

momentum energies $\sqrt{s} \sim 1.3$ GeV, which promptly decays into pions [44]:

$$\mathrm{p} + \gamma \rightarrow \Delta^{+} \rightarrow \mathrm{p} + \pi^{0}, \tag{2.26a}$$

$$\mathrm{p} + \gamma \rightarrow \Delta^{+} \rightarrow \mathrm{n} + \pi^{+}. \tag{2.26b}$$

Although the total cross section for pγ scattering is much lower than σ_{pp} (Figure 2.3), typical thermal photon backgrounds are much denser than proton outflows. In extremely luminous environments, photopion production is thus expected to dominate CR cooling above the kinematic threshold, $E_{\gamma} \sim m_{\pi}c^{2}[1 + m_{\pi}/(2m_{\mathrm{p}})] \sim 145$ MeV [14].

In principle, the cooling time scale associated to the production of a particle i in pγ interactions could be calculated with an expression similar to (2.24), replacing the outflow density n_{out} with the density of the photon background and σ_{pp} by the production cross section σ_{i}. The total photomeson cooling time would then become a sum over stable secondaries and tertiary decay products:

$$\begin{aligned} t_{\mathrm{c,p}\gamma}(E_{\mathrm{p}}) &= E_{\mathrm{p}} \left[\sum_{i} \left(\int_{m_i c^2}^{\infty} dE_{\mathrm{i}} \mathcal{P}_{i}(E_{\mathrm{p}}, E_{i}) \right) \right]^{-1}, \\ &\sim E_{\mathrm{p}} \left[\sum_{i} \int_{0}^{\infty} dE_{i} \int_{0}^{\infty} d\epsilon c \rho_{\gamma}(\epsilon) \sigma_{i}(E_{\mathrm{p}}, E_{i}) \right]^{-1}. \end{aligned} \tag{2.27}$$

The largest contributions to the sum are expected to come from the decay products of π^{+} and π^{0}. However, the production of $\pi^{+}\pi^{-}$ pairs is also possible at high energies, so e^{-} and $\overline{\nu}_{\mathrm{e}}$ production must also be accounted for [14].

2.3.2 (Photo)Hadronic interactions II: Bethe-Heitler pair production

Below the photomeson production threshold, CRs may cool in interactions with thermal photons via electron-positron pair production:

$$\mathrm{p} + \gamma \rightarrow \mathrm{p} + \mathrm{e}^{-} + \mathrm{e}^{+}, \tag{2.28}$$

which requires a minimum energy $E_\gamma \sim 2m_\mathrm{e}c^2$ in the proton rest frame. The differential cross-section for this process in the Born approximation is given in [45] and quoted in Appendix C. The spectral electron-positron production rate for the scattering of a proton with Lorentz factor γ_p on a gray-body distribution of photons with temperature T and normalization constant A:

$$\rho(E_\gamma) = A\frac{E_\gamma^2}{e^{\frac{E_\gamma}{k_\mathrm{B}T}} - 1} \tag{2.29}$$

may then be calculated via [14]:

$$\frac{d^2 n_\mathrm{e}}{dt d\epsilon_\mathrm{e}} = -\frac{A k_\mathrm{B} T}{2\gamma_\mathrm{p}^3} \int_{\frac{(\gamma_p+\epsilon_\mathrm{e})^2}{2\gamma_p \epsilon_\mathrm{e}}}^{\infty} d\epsilon \epsilon \ln\left(1 - e^{-\epsilon/(2\gamma_\mathrm{p} kT)}\right) \int_{\frac{\gamma_\mathrm{p}^2+\epsilon_\mathrm{e}^2}{2\gamma_\mathrm{p}\epsilon_\mathrm{e}}}^{\epsilon-1} \frac{d\epsilon_-}{p_-} \left.\frac{d^2\sigma}{d\epsilon_- \cos\theta_-}\right|_{\cos\theta_- = \frac{\gamma_\mathrm{p}\epsilon_- - \epsilon_\mathrm{e}}{\gamma_\mathrm{p} p_-}}, \tag{2.30}$$

where $\epsilon_\mathrm{e} \equiv E_\mathrm{e}/m_\mathrm{e}c^2$ is the normalized lepton energy in the observer frame, $\epsilon_- \equiv E_-/m_\mathrm{e}c^2$, $p_- \equiv P_-/m_\mathrm{e}c^2$, θ_- and and $\epsilon \equiv E_\gamma/m_\mathrm{e}c^2$ are the normalized energy and momentum of the lepton, the lepton-photon angle and the normalized photon energy in the proton rest frame. The limits of the integrals follow from kinematic cuts.

The cooling time scale of a proton with energy E_p can be computed from this result as:

$$t_\mathrm{c,bh}(E_\mathrm{p}) = \frac{2m_\mathrm{e}}{E_\mathrm{p}} \int_1^{+\infty} d\epsilon_\mathrm{e} \epsilon_\mathrm{e} \frac{d^2 n_\mathrm{e}}{dt d\epsilon_\mathrm{e}}, \tag{2.31}$$

where the factor 2 accounts for the production of both an electron and a positron.

2.3.3 Inverse Compton scattering

A photon with sufficient momentum may cause a charge at rest to recoil upon collision. In the observer frame, either particle may gain energy as a result, depending on the Lorentz factor γ. Relativistic charges can thus cool by colliding with background radiation, which is called inverse Compton (IC) scattering. When $\gamma\epsilon < m_\mathrm{e}c^2$, i.e. photon energy ϵ in the rest frame of the electron is low, IC occurs in the Thomson regime; at $\gamma\epsilon > m_\mathrm{e}c^2$, the photon may lose energy in the rest frame as a result of the collision, and other quantum effects yield significant corrections to the cross section that reduce the efficiency of the cooling: this is commonly referred to as the Klein-Nishina regime [46].

Assuming isotropic distributions of both charges and photons, the differential cross section for the process is given by the Klein-Nishina formula, averaged over the initial photon polarizations and summed over the final photon polarizations [47]:

$$\sigma(E_\gamma, \epsilon, \gamma) = \frac{3\sigma_T}{4\epsilon\gamma^2}\left[2q\ln q + (1+2q)(1-q) + \frac{(\Gamma_e q)^2(1-q)}{2(1+\Gamma_e q)}\right], \tag{2.32}$$

where $\sigma_{\rm T} = (8\pi/3)[e^2/(mc^2)]^2$ is the Thomson cross section, ϵ and E_γ are the photon energies before and after scattering, and:

$$\Gamma_e = \frac{4\epsilon\gamma}{mc^2}, \quad q = \frac{E_\gamma}{\Gamma_e(\gamma mc^2 - E_\gamma)}. \tag{2.33}$$

The value of q is kinematically restricted to $1 \geq q \geq 1/(4\gamma^2)$.

Charges with very high energies E may lose large fractions of their energy with each collision, so at the high end of the spectrum inverse Compton cooling approaches a discrete energy loss. Regardless, an effective cooling time scale may still be defined as:

$$t_{\rm c,ic}(E) = E\left[\int dE_\gamma \mathcal{P}_{\rm IC}(E_\gamma, E)\right]^{-1} = E\left[\int_0^\infty dE_\gamma \left(cE_\gamma \int_0^\infty d\epsilon \rho_\gamma(\epsilon)\sigma(E_\gamma, \epsilon, E)\right)\right]^{-1}, \tag{2.34}$$

where $\rho_\gamma(\epsilon)$ is the density of target photons. The function $\mathcal{P}_{\rm IC}(E_\gamma, E)$ estimates the spectral power loss due to the upscattering of background photons to energies E_γ, under the assumption that $E_\gamma \gg \epsilon$.

2.3.4 Radiative cooling I: synchrotron emission

Accelerated charges continuously lose energy, which in the relativistic regime may be treated semiclassically as the result of Compton scattering on virtual photons [48]. The emission caused by interactions with a uniform magnetic field is called synchrotron radiation.

The shape of the synchrotron spectrum stems from the relativistic beaming of the emitted photons along the direction of motion of the particle. Distant observers only receive periodic pulses of light, which last as long as the alignment between the beaming cone and their field of view; broadening

effects in transport then turn the Fourier transform of the intermittent time signal into a continuous function [49].

The spectral synchrotron power $\mathcal{P}_{\text{syn}}$ emitted by a single relativistic electron with Lorentz factor γ may be parametrized in terms of:

$$x \equiv \frac{2\omega}{3\omega_B \gamma^2}\left[1+\left(\frac{\gamma\omega_p}{\omega}\right)^2\right]^{3/2}, \tag{2.35}$$

where $\omega_{\text{B}} = eB/m_{\text{e}}c$ is the cyclotron frequency of an electron in a magnetic field B and ω_{p} is the typical frequency of the plasma (Appendix A.2). The result, summed over photon polarizations, is [47]:

$$\mathcal{P}_{syn}(x,\theta) \simeq \frac{1}{4\pi}\left(\frac{3}{8\pi}\sigma_{\text{T}}\right)^{1/2}\frac{eB}{\hbar}x\int_{\frac{x}{\sin\theta}}^{\infty} dz K_{5/3}(z), \tag{2.36}$$

where $K_{5/3}(z)$ is a modified Bessel function of the second kind and θ is the angle between the magnetic field and the observer. In analogy with (2.34), this yields a cooling time scale:

$$t_{\text{c,syn}}(E) \sim E\left[\int_0^{\infty} d(\hbar\omega)\mathcal{P}_{\text{syn}}(x,\theta)\right]^{-1}. \tag{2.37}$$

Unlike $\mathcal{P}_{\text{syn}}$, $t_{\text{c,syn}}$ does not depend on the viewing angle, because the second integral runs over all values of x.

2.3.5 Radiative cooling II: bremsstrahlung

Like synchrotron radiation, bremsstrahlung can be treated as the Compton scattering of a charged particle with the virtual photons of an external field. In the dipole approximation, the scattering amplitude of pp and ee Bremsstrahlung vanishes [46], so the relevant emission is that of electrons or positrons deflected by the electric field of protons or ions. In the Born approximation, the differential cross section in a fully-ionized plasma is then [47]:

$$\sigma(\epsilon, E_{\text{e}}) = \frac{3}{8\pi}\alpha\sigma_{\text{T}}\left\{\left[1+\left(1-\frac{\epsilon}{E_{\text{e}}}\right)^2\right]-\frac{2}{3}\left(1-\frac{\epsilon}{E_{\text{e}}}\right)\right\}\phi_{\text{u}}, \tag{2.38}$$

$$\phi_{\text{u}} = 4\left\{\ln\left[\frac{2E_{\text{e}}}{m_{\text{e}}c^2}\left(\frac{E_{\text{e}}-\epsilon}{\epsilon}\right)\right]-\frac{1}{2}\right\}, \tag{2.39}$$

where α is the fine-structure constant. Hence, the electron cooling time scale in a proton outflow with density n_{out} can be calculated via:

$$t_{\mathrm{c,brems}}(E_{\mathrm{e}}) = E_{\mathrm{e}}\left[\int_0^\infty d\epsilon \mathcal{P}_{Brems}(\epsilon, E_{\mathrm{e}})\right]^{-1} = E_{\mathrm{e}}\left[\int_0^\infty d\epsilon c\epsilon n_{out}\sigma(\epsilon, E_{\mathrm{e}})\right]^{-1}. \tag{2.40}$$

2.4 Fokker-Planck equation

This section is intended to motivate a mathematical description of the dynamics of the particles that are accelerated in the environment of an SMBH over the lifetime of the transient. The competition between energy gains and losses may be formulated as a time-dependent Boltzmann transport equation in phase space [50]:

$$\begin{aligned}\frac{\partial f}{\partial t}(t,\mathbf{p}) = &\frac{Q_{\mathrm{in}}}{4\pi|\mathbf{p}|^2}(t,\mathbf{p}) - \frac{Q_{\mathrm{out}}}{4\pi|\mathbf{p}|^2}(t,\mathbf{p}) \\ &+ \frac{1}{4\pi|\mathbf{p}|^2}\int d^3(\delta p)[\mathcal{R}(t,\mathbf{p},\mathbf{p}+\delta\mathbf{p})f(t,\mathbf{p}+\delta\mathbf{p}) - \mathcal{R}(t,\mathbf{p}-\delta\mathbf{p},\mathbf{p})f(t,\mathbf{p})],\end{aligned} \tag{2.41}$$

where $f(t,\mathbf{p})$ is the spatially-averaged phase-space density of particles with momentum $\mathbf{p}$, $Q_{\mathrm{in}}/(4\pi|\mathbf{p}|^2)$ is the injection rate of primary particles, $Q_{\mathrm{out}}/(4\pi|\mathbf{p}|^2)$ is the escape rate, and $\mathcal{R}(t,\mathbf{p},\mathbf{p}_1)$ is the spectral rate at which secondary particles with momentum $\mathbf{p}$ are produced during the scattering of particles with momentum $\mathbf{p}_1$.

The integral term therefore represents the net scattering rate onto states with momentum $\mathbf{p}$. If $\mathcal{R}$ is a narrow distribution such that the dominant contributions to the integral come from $|\delta\mathbf{p}| \ll |\mathbf{p}|$, the integrand can be expanded around $\mathbf{p} \pm \delta\mathbf{p} \simeq \mathbf{p}$ to arrive at:

$$\begin{aligned}\frac{\partial f}{\partial t}(t,\mathbf{p}) \simeq &\frac{Q_{\mathrm{in}}}{4\pi|\mathbf{p}|^2}(t,\mathbf{p}) - \frac{Q_{\mathrm{out}}}{4\pi|\mathbf{p}|^2}(t,\mathbf{p}) \\ &+ \frac{1}{|\mathbf{p}|^2}\int d^3(\delta p)\sum_i \frac{\partial}{\partial p_i}\left\{f(t,\mathbf{p})(\delta p_i)\mathcal{R}(t,\mathbf{p},\mathbf{p}+\delta p_i\mathbf{e}_i)\right]_{\delta p_i=0} \\ &+ \frac{1}{|\mathbf{p}|^2}\sum_{i,j}\int d^3(\delta q)\frac{\partial^2}{\partial p_i \partial p_j}\left[f(t,\mathbf{p})\frac{1}{2}(\delta p_i)(\delta q_j)\mathcal{R}(t,\mathbf{p},\mathbf{p}+\delta p_i\mathbf{e}_i+\delta q_j\mathbf{e'}_j)\right]_{\delta p_i=\delta q_j=0},\end{aligned} \tag{2.42}$$

where $\mathbf{e}_i$, $\mathbf{e'}_j$ are unit vectors along the axes i, j. The first derivative and second derivatives represent advective and diffusive processes in momentum space, respectively: this kind of expression is often called a Fokker-Planck equation (e.g. [51]). Diffusion in momentum space is associated with processes such as isotropic scattering with magnetic clouds, so it can be neglected in environments where DSA is the main mechanism of particle acceleration, because it leads to much lower fractional energy gains.

For fully isotropic particle transport, the terms in (2.42) depend only on $|\mathbf{p}| \equiv p$. It is then trivial to integrate both sides of the equation over the solid angle Ω to obtain a factor 4π. Furthermore, the production of TeV-PeV neutrinos requires the particles in the source to be ultra-relativistic, $E \sim pc$. Using the definitions:

$$\mathcal{R}(\mathbf{p}, \mathbf{p} + \delta p_i \mathbf{e}_i) \equiv \frac{\mathcal{R}(p, p + \delta p)}{4\pi}, \tag{2.43}$$

$$4\pi E^2 f(t, E) \equiv n(t, E), \tag{2.44}$$

and $d^3(\delta p) = p^2 d(\delta p) d\Omega$ to carry out the remaining angular integral on the right-hand side, the equation then becomes:

$$\begin{aligned} \frac{dn(t,E)}{dt} &\simeq Q_{\text{in}}(t,E) - Q_{\text{out}}(t,E) \\ &+ \frac{\partial}{\partial E}\left[n(t,E)\int d(\delta E)(\delta E)\mathcal{R}(t,E,E+\delta E)\right] + \mathcal{O}(\delta E^2), \end{aligned} \tag{2.45}$$

The product $(\delta E)\mathcal{R}$ is the total rate of interactions that lead to momentum exchanges δE, so the integral in brackets is essentially an emitted power $\mathcal{P}(t, E)$. The advection term thus represents that particles in the environment of the SMBH with spectral density $n(t, E)$ cool via continuous energy losses on a time scale $t_{\text{c}} \sim E/\mathcal{P}(t, E)$.

3 Model of high-energy emission from Tidal Disruption Events

In this work, it is assumed that the interactions that lead to neutrino and electromagnetic emission from TDEs take place in a spherical radiation zone around the SMBH, filled with homogeneous photon and proton backgrounds. Primary protons and electrons are injected homogeneously and isotropically into this region and cool via inelastic collisions and radiative processes. These dynamics are treated numerically using the space-averaged Fokker-Planck equation in the ultra-relativistic limit (2.45) .

In Section 3.1, typical scales of the size of the radiation zone and the target densities of protons and photons are discussed; in Section 3.2, the injection spectra of primary protons and electrons are defined; in Section 3.3, the numerical treatment of the Fokker-Planck equation is explained, with special reference to the implementation of (photo)hadronic interactions. The fiducial values used in the model are collected in Appendix B.1.

3.1 Radiation zone and scattering backgrounds

3.1.1 Definition and size of the radiation zone

The radiation zone is the environment surrounding the SMBH where scattering events between high-energy particles and low-energy backgrounds can lead to efficient production of astronomical messengers. Thus, in order to calculate e.g. the neutrino fluence on Earth from a TDE, it is first necessary to estimate its typical size (R).

The typical neutrino energy from pion decay is related to the primary CR energy E_p via [18]:

$$\langle E_\nu \rangle \sim 0.05 E_\mathrm{p}, \tag{3.1}$$

so for the production of 100 TeV astrophysical neutrinos, primary protons with $E_\mathrm{p} \gtrsim 2$ PeV are required. CRs with $\mathcal{O}(1-10)$ PeV energy are thus required to remain magnetically confined within the radiation zone over the duration of the TDE t_dyn. This means that R should be larger than the Larmor radius (2.20) and the distance that protons may travel diffusively during this period, $\sqrt{D_\mathrm{Bohm} t_\mathrm{dyn}}$. The former is smaller than the latter, so both conditions reduce to:

$$R \gtrsim \sqrt{D_\mathrm{Bohm} t_\mathrm{dyn}} \sim 3 \times 10^{15}\ \mathrm{cm} \left(\frac{E_\mathrm{p}}{\mathrm{PeV}}\right)^{1/2} \left(\frac{B}{\mathrm{G}}\right)^{-1/2} \left(\frac{t_\mathrm{dyn}}{1000\ \mathrm{d}}\right)^{1/2}. \tag{3.2}$$

The time scale t_dyn is defined as the period with $\dot{M}(t)c^2 > L_\mathrm{edd}$, because the phenomenology of the source, e.g. the accretion regime, is expected to change once accretion drops below the Eddington level [18].

Successful fits of electromagnetic spectra from TDEs could support the use of values $R \gtrsim 10^{15}$ cm as a benchmark. Since the emitted power [(2.34), (2.36), (2.40)] depends on the Lorentz factor γ, radiation is expected mainly from the region where particle energies are highest, and therefore it should be dominated by X-ray photons from the accretion disc, both thermal and upscattered via inverse Compton collisions with a hot electron corona [52]. Observations in OUV bands can thus be explained by an outer thermal photosphere which reprocesses part of the X-rays [53], and whose radius R_phos could match $R_\mathrm{phos} \sim 10^{15}$ cm (Appendix B.1).

The expectation of photopion production by CRs with energies of few PeV is also consistent with a high in-source X-ray luminosity. Adopting (3.1) into the definition of $\sqrt{s}$ and looking for the maximum of the photomeson production cross section (Figure 2.3, also [54]) yields an estimate of the the optimal photon energy E_γ for $\langle E_\nu \rangle$-neutrino production. When the target background is thermal, the result can be related to the photon temperature T by taking into account that cooling is most efficient at the maximal density, given by $E_\gamma \simeq 2.8 k_\mathrm{B} T$. Inverting (3.1) finally yields a relation between T and E_p [18]:

$$E_\mathrm{p} \sim 160\ \mathrm{PeV} \left(\frac{k_\mathrm{B} T}{\mathrm{eV}}\right)^{-1}, \tag{3.3}$$

which for $E_{\rm p} \sim 2$ PeV implies a thermal X-ray target ($k_{\rm B}T \sim 80$ eV).

To simplify comparisons with the literature, a spherical radiation zone with fiducial size $R = 5 \times 10^{15}$ cm and magnetic field $B = 1$ G is considered in the calculations. These values are taken from Figure 2 in [18]. The use of G-scale values of the magnetic field at $R \sim 10^{15}$ cm is motivated by simulations of TDEs that report fluxes $\sim 10^{31}$ G cm^{-2} at a distance $20GM_{\bullet}/c^2$ from the SMBH [55].

3.1.2 Normalization of the scattering backgrounds

Neutrinos produced in interactions of CRs with proton (pp) and low-energy radiation (pγ) backgrounds in the radiation zone (Figure 3.1), which are assumed to be homogeneous. Below, motivation is given for the parameters that define the nature of these targets.

The estimate (2.14) implies that $\dot{M}(t)$ will be super-Eddington for a period of several years following disruption. The excess of mass will be driven away from the SMBH as an almost isotropic outflow [56], whose density can be estimated to be [18]:

$$n_{\rm out}(t) \equiv \frac{\varepsilon_{\rm out}\dot{M}(t)c^2}{\frac{4}{3}\pi R^3 m_{\rm p}} \left[\frac{R}{c}\frac{c}{3v_{\rm out}}\right]. \tag{3.4}$$

Here, $\varepsilon_{\rm out}$ is the conversion efficiency of accreting mass into the outflow, and the factor in brackets estimates the wind escape time: $t_{\rm fs} \equiv R/c$ is the free-streaming time in the radiation zone, and the factor $c/(3v_{\rm out})$ corrects for optical thickness. These protons, along with a minor contribution from outflows produced during fallback, could be a feasible target for pp interactions with CRs.

The normalization factor $\dot{M}(0)$ in (2.15) constrains the velocity of the outflow. For $\dot{M}(0)c^2 \sim \mathcal{O}(10-100)L_{\rm edd}$, as predicted by (2.10) and (2.11), $v_{\rm out} \sim 0.1c$ is expected. However, a near-vacuum along the disc's rotation axis, sustained by centrifugal repulsion and radiation pressure, could act as a funnel to eject matter at higher speeds, $v_{\rm fun} \sim 0.4c$ [55, 57].

Observations of electromagnetic emissions from TDEs suggest that the targets for photomeson production should be modelled as separate X-ray and OUV gray-body spectra $\rho(E_\gamma)$ (2.29) [10, 11]. These backgrounds are normalized to the observed bolometric luminosities (L_γ) in their respective energy ranges:

$$\int dE_\gamma E_\gamma \rho(t, E_\gamma) = \frac{L_\gamma(t)}{\frac{4}{3}\pi R^3} \frac{t_{\mathrm{fs}}}{3}. \tag{3.5}$$

Interactions with an IR echo from OUV photons reprocessed in a dust torus around the SMBH are also possible, but likely subdominant, as they require very high proton energies. This background is normalized like (3.5), but using the size of the dust cloud instead of R. Estimates of the IR luminosity and the torus radius are taken from [18] and shown in Appendix B.1.

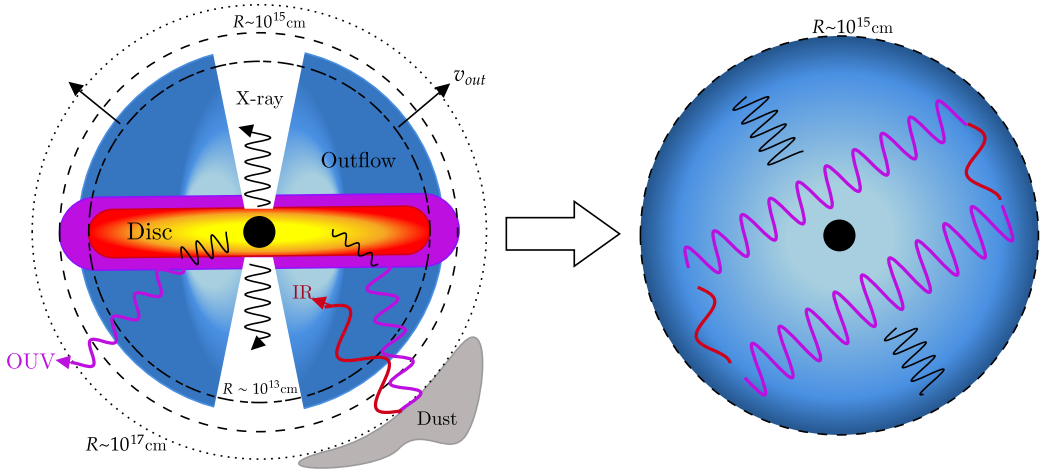

Figure 3.1.: Homogeneous and isotropic radiation zone, where CRs cool via interactions with low-energy radiation and protons.

3.2 Injection of non-thermal particles

3.2.1 Assumption on the injection spectrum

Under the assumptions of isotropy and small energy losses per collision, the behaviour of the advective term in the Fokker-Planck equation is well-understood in terms of continuous cooling. The typical inelasticity of resonant photopion production is $K_{\mathrm{p}\gamma} \sim 0.2$ [58], Bethe-Heitler cooling usually leads to relative losses of order $K_{\mathrm{bh}} \sim m_{\mathrm{e}}/m_{\mathrm{p}}$ [59], and $K_{\mathrm{pp}} \sim 0.5$ as already discussed. The continuous energy loss approximation is thus expected to be reasonably

accurate for predictions of neutrino production at PeV CR energies, where pp interactions are subdominant.

The rates of the individual energy-loss mechanisms, given by (2.24), (2.27), (2.31), (2.34), (2.37) and (2.40), have been summed to yield an effective cooling rate:

$$t_{\mathrm{c}}^{-1} \sim (\sum t_{\mathrm{c},i}^{-1}). \tag{3.6}$$

If $t_c^{-1} \ll t_{\mathrm{acc}}^{-1}$, the injection term Q_{in} may be approximated by:

$$Q_{\mathrm{in}}(t, E) = Q_0(t) E^{-2} \exp\left(-\frac{E}{E_{\mathrm{max}}(t)}\right), \tag{3.7}$$

because DSA will lead to a power-law distribution (2.18) regardless of the spectrum of accreting mass, which carries large uncertainties. Here, $E_{\mathrm{max}}(t)$ is the maximum energy the particles can be accelerated to in a time t, and $Q_0(t)$ is a time-dependent normalization function. There is no spatial dependence because (2.45) describes average densities.

3.2.2 Estimation of the high-energy cut-off

The exponential cut-off $E_{\mathrm{max}}(t)$ in the primary spectrum is set at every instant t by the condition:

$$t_{\mathrm{acc}}(t, E_{\mathrm{max}}) = \min\left[t, t_{\mathrm{esc}}(E_{\mathrm{max}}), t_{\mathrm{c}}(t, E_{\mathrm{max}})\right]. \tag{3.8}$$

High-energy primaries typically remain in the radiation zone for a period $t \lesssim t_{\mathrm{esc}}$ before escaping, either free streaming or diffusively. This sets a time-independent upper bound for the cut-off energy [18]:

$$t_{\mathrm{esc}} \sim \max\left[\frac{R}{c}, \frac{R^2}{D_{\mathrm{Bohm}}}\right] \tag{3.9}$$

On the other hand, cooling is inefficient over short periods, so if $t < t_{\mathrm{c}}(t)$, E_{max} is simply given by the maximum time t the particles may have spent in this region. Finally, if $t_{\mathrm{c}} < t < t_{\mathrm{esc}}$, the cut-off lies at the energy where the acceleration and cooling rates are equal.

3.2.3 Normalization of the primary injection spectra

Comparison of the acceleration and viscous time scales shows that DSA is almost instantaneous relative to energy dissipation in the disc. Indeed, the typical DSA time scale for Bohm diffusion can be written as:

$$t_{\mathrm{acc}} \sim 293 \text{ s} \left(\frac{E}{\mathrm{PeV}}\right) \left(\frac{B}{\mathrm{G}}\right) \left(\frac{v_{\mathrm{out}}}{c}\right)^{-2}, \tag{3.10}$$

which is $t_{\mathrm{acc}} \sim 3$ s for the fiducial value $v_{\mathrm{out}} \sim 0.1c$. Thus, acceleration is instantaneous compared to viscous dissipation and the injection of non-thermal particles into the radiation zone can be assumed to follow $\dot{M}$. This result is qualitatively independent of improvements in the model of disruption which might influence the parameters of the disc, because the orders of magnitude involved are too different. Hence, $Q_{\mathrm{in}}(t)$ can be normalized via:

$$Q_{0i}(t) \int_{m_{\mathrm{p}}c^2}^{\infty} dE E \left[E^{-2} \exp\left(-\frac{E}{E_{\mathrm{max}}(t)}\right)\right] = \frac{\varepsilon_{\mathrm{nt}} \varepsilon_i \dot{M}(t) c^2}{\frac{4}{3}\pi R^3}. \tag{3.11}$$

Using the definition (2.15), $Q_{\mathrm{in}}(t)$ scales in time like the OUV luminosity. $\varepsilon_{\mathrm{nt}}$ is the conversion efficiency of accreting mass into non-thermal particles, and ε_i is the relative luminosity of each type of accelerated particle. In this work, the injection of both primary protons $Q_{\mathrm{p}}(t, E_{\mathrm{p}})$ and electrons $Q_{\mathrm{e}}(t, E_{\mathrm{e}})$ is considered. Studies of starburst-galaxy nuclei (e.g. [60]) suggest $\varepsilon_{\mathrm{e}} = \varepsilon_{\mathrm{p}}/50$ and this value is used throughout.

3.3 Numerical treatment of the Fokker-Planck equation and calculation of secondary spectra

At the beginning of each event, primary electrons and protons accelerated via DSA, $Q_{\mathrm{p,e;nt}}$ (3.7) are injected into the radiation zone. Their evolution is described with a transport equation (2.45), where the cooling rate t_{c}^{-1} (3.6) is set by the radiative and scattering processes discussed in Section 2.3.

Therefore, the spectral proton and electron densities $n_{\mathrm{p,e}}(t, E)$ were calculated at each instant t by solving:

$$\frac{\partial n_{\mathrm{p,e}}}{\partial t}(t, E) = Q_{\mathrm{p,e;nt}}(t, E) + \frac{\partial}{\partial E}\left[\frac{E}{t_{\mathrm{c}}(t, E)} n_{\mathrm{p,e}}(t, E)\right] - \frac{n_{\mathrm{p,e}}}{t_{\mathrm{esc}}}(t, E) \tag{3.12}$$

numerically in Python, using an upwind scheme appropriate for advection-dominated equations [61].

The solutions were then folded with production cross sections to calculate the secondary spectra emitted by the studied TDEs. Charged pion decay (2.23a) as a result of photomeson production and pp scattering, as well as Bethe-Heitler pair production (2.28), results in the creation of electrons and positrons that can also interact with the target backgrounds ($Q_{\mathrm{e,p}\gamma}$, $Q_{\mathrm{e,pp}}$ and $Q_{\mathrm{e,bh}}$, respectively), but if electron-electron interactions remain negligible, an overall injection term:

$$Q_{\mathrm{e}} \equiv \sum Q_{\mathrm{e,nt}} + Q_{\mathrm{e,bh}} + Q_{\mathrm{e,pp}} + Q_{\mathrm{e,p}\gamma} \tag{3.13}$$

can be adopted into (3.12) to calculate the total electron density.

Interactions between charged particles and their own synchrotron and bremsstrahlung photons, as well as with radiation upscattered via inverse Compton cooling, are more problematic. If the luminosity generated by these processes is comparable to the backgrounds, secondary photons would become a target for photomeson production or inverse Compton cooling, which could significantly alter the neutrino fluence and the electromagneitc spectrum. Such corrections are outside the scope of this project, so it has been assumed that secondary photons do not significantly alter the in-source densities $n_{\mathrm{p,e}}$. The bolometric luminosity of the background is compared with electron emissions from radiative and IC cooling in Appendix C. Lepton cooling yields a sub-dominant contribution to the target density in AT2019dsg and AT2019fdr, so large corrections to the results in the linear regime are unlikely in these TDEs. On the contrary, electron-radiated and inverse Compton photons dominate in AT2019aalc by almost an order of magnitude. Possible deviations from the results in this work are discussed in the Appendix.

The production cross sections (σ_i) of secondary $\mathrm{e^+e^-}$, neutrinos and photons from pp interactions have been obtained using the Python package AAFRAGPY

[62]. In the primary energy range $E_{\rm p} > 4$ GeV, these are implemented as an interpolation of results from a Monte Carlo event generator, whose model parameters were fit to LHC data; below this threshold, the analytic parametrizations in [42] are used instead. On the other hand, the distributions of secondaries from photomeson production were calculated using the analytic parametrizations in [14]. For a given CR spectrum $n_{\rm p}$ and and photon background ρ_γ, the spectral production rate of a secondary i is then:

$$Q_{\rm i}(E_{\rm i}, t) = c \int \frac{dE_{\rm p}}{E_{\rm p}} dE_\gamma n_{\rm p}(E_{\rm p}, t) \rho_\gamma(E_\gamma, t) \sigma_i(E_{\rm i}, E_{\rm p}, E_\gamma), \tag{3.14}$$

which includes the production of electrons and positrons $Q_{\rm e;pp,p\gamma}$. Below the photomeson production threshold, the Bethe-Heitler pair production rate $Q_{\rm e,bh}$ is given by (2.31).

4 Multi-wavelength and neutrino emission from Tidal Disruption Events

This chapter reports and discusses the multi-wavelength and neutrino signals from TDEs AT2019dsg, AT2019fdr and AT2019aalc. Section 4.1 is dedicated to the estimation of the high-energy cut-off in the injection spectra of primary protons and electrons. In Section 4.2, the numerical solutions of the transport equation under the conditions described in Chapters 2 and 3 are presented. In Section 4.3, the electromagnetic spectrum resulting from the radiative and IC cooling of electrons is presented, analysed in search of evidence of (photo)hadronic interactions in the sources, and compared with observational detection limits. Finally, the neutrino fluences from the three TDEs are discussed in Section 4.4.

4.1 High-energy cut-off in the injection spectra

4.1.1 Comparison of acceleration and (photo)hadronic cooling time scales

The relations (3.1) and (3.3) imply that efficient production of 100 TeV neutrinos from a proton injection spectrum (3.7) requires $E_{\rm p,max}(t) \gtrsim 10^6$ GeV at some instant t during the super-Eddington phase and before high-energy protons can escape the radiation zone. The cut-off in the primary spectrum is given by (3.8), so this condition is met if:

$$\left.\begin{aligned} t_{\rm acc} < t_{\rm c} < t \\ t < \min[t_{\rm dyn}, t_{\rm esc}] \end{aligned}\right\} \tag{4.1}$$

where all terms are evaluated at $E_\mathrm{p} \sim 10^6$ GeV) and time t. t_acc and t_esc only depend on free parameters of the model, which are time-independent and common to all sources. The fiducial values in Appendix B.1 lead to $t_\mathrm{acc}(E_\mathrm{p} \lesssim 10^7 \text{ GeV}) < t_\mathrm{c}$ during all TDEs, as shown in Figure 4.1. Therefore, populations of protons that evolve according to (3.12) can feasibly produce high-energy neutrinos within the lifetime of the transients.

Figure 4.2 shows the evolution of the cut-off over t_dyn in more detail. Cooling can not compete with DSA unless $t_\mathrm{c} < t$, and the absolute minimum of t_c is initially of order $t \gtrsim 10^4$ s (AT2019fdr) or $t \gtrsim 10^5$ s (AT2019dsg, AT2019aalc). Furthermore, this minimum is given by interactions with the OUV target, so it increases over time as the background fades. As a result, $E_\mathrm{p,max}$ is simply set by $t_\mathrm{acc}(E_\mathrm{p,max}) \sim t$ for a period of a few days after the optical peak, according to (3.8).

When $t_\mathrm{c} < t$, energy losses become dynamically relevant and the time evolution of $E_\mathrm{p,max}(t)$ slows down. In AT2019fdr, the backgrounds are luminous enough that the cut-off is set by $t_\mathrm{acc}(E_\mathrm{p,max}) = t_\mathrm{c}(E_\mathrm{p,max})$ for the remainder of the event. On the contrary, the cut-off plateaus to a constant value $E_\mathrm{p,max} \sim 2 \times 10^8$ GeV in the latter half of AT2019dsg and AT2019aalc, because EeV CRs diffuse out of the radiation zone before they can cool.

Furthermore, the shape of t_c already gives some indication on the time dependence of the emitted neutrino flux. Protons cool on time scales $t_\mathrm{pp} \gtrsim 10^8$ s (inelastic scattering) and $t_{\mathrm{c},\mathrm{p}\gamma} \gtrsim 10^5$ s (photomeson production). Along with the condition $t_\mathrm{c} < t$ in (4.1), production times $t \sim \mathcal{O}(100)$ d [18] thus suggest that the observed neutrinos have a photohadronic origin.

The inelastic pp scattering and Bethe-Heitler pair production time scales are too large to compete with proton acceleration, but they are relevant for the production of secondary neutrinos and charged leptons.

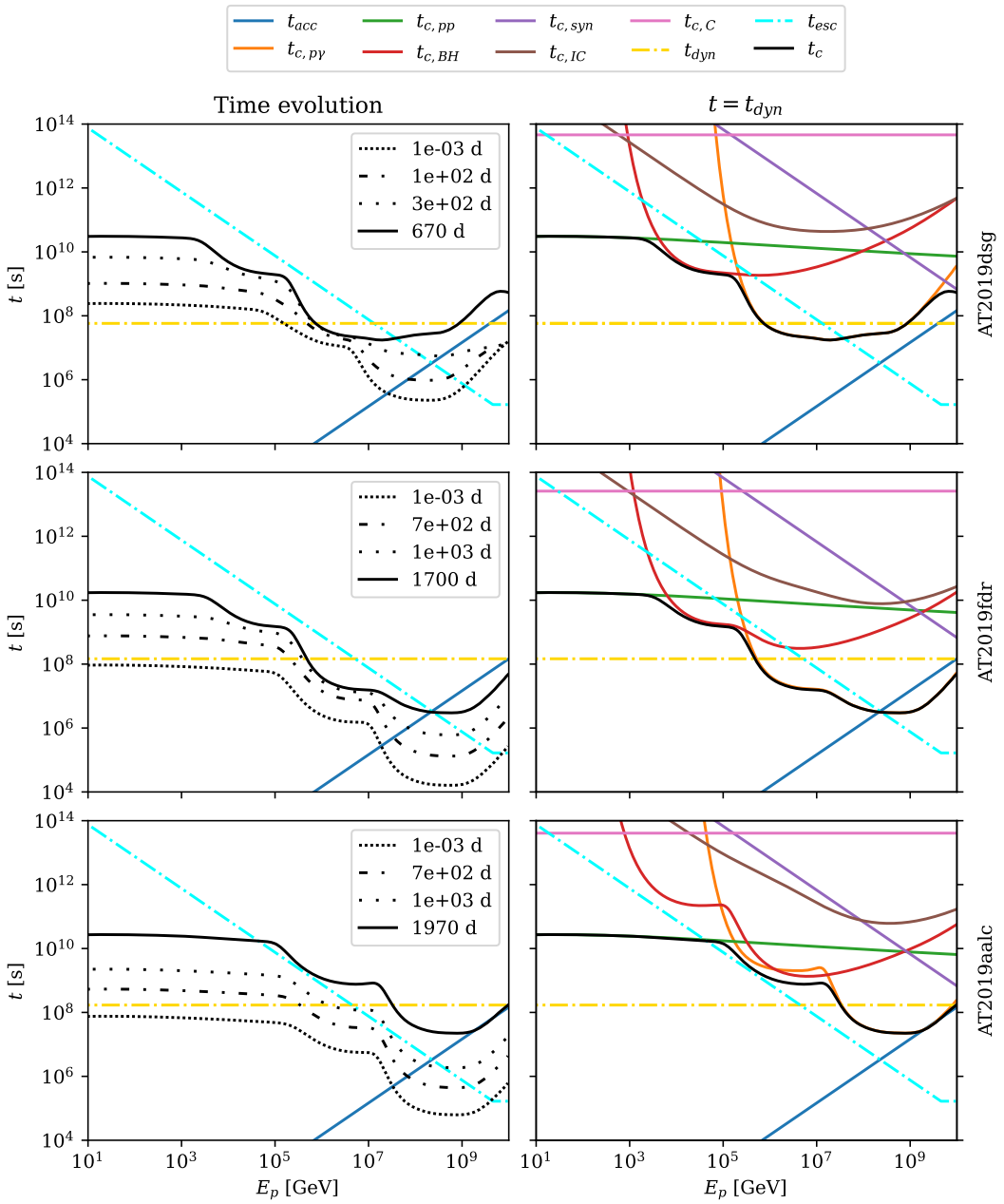

Figure 4.1.: Proton cooling time scales with respect to proton energy E_p. Left: total cooling time scale (t_c, black) over the lifetime (t_dyn, golden dash-dotted) of the sources, compared with the DSA time scale (t_acc, dark blue) and the escape time (t_esc, cyan dash-dotted). Right: Individual cooling time scales at $t = t_\mathrm{dyn}$.

$t_\mathrm{c,pp}$ is approximately energy-independent, because σ_pp increases logarithmically above the kinematic threshold and the proton target is cold gas. However, this process is subdominant for primary proton energies $E_\mathrm{p} \gtrsim 10^5$ GeV, where photohadronic interactions are much more efficient. In addition, the depen-

dence of n_{out} on the accretion rate (3.4) makes $t_{\text{c,pp}}$ increase uniformly over time, and as a result $t_{\text{c,pp}} > t_{\text{dyn}}$ for most of the super-Eddington phase. Hence, its contribution to the fluxes of secondary electrons is likely minor compared to Bethe-Heitler pair production or photomeson production, although it could dominate the low-energy end of the neutrino spectrum.

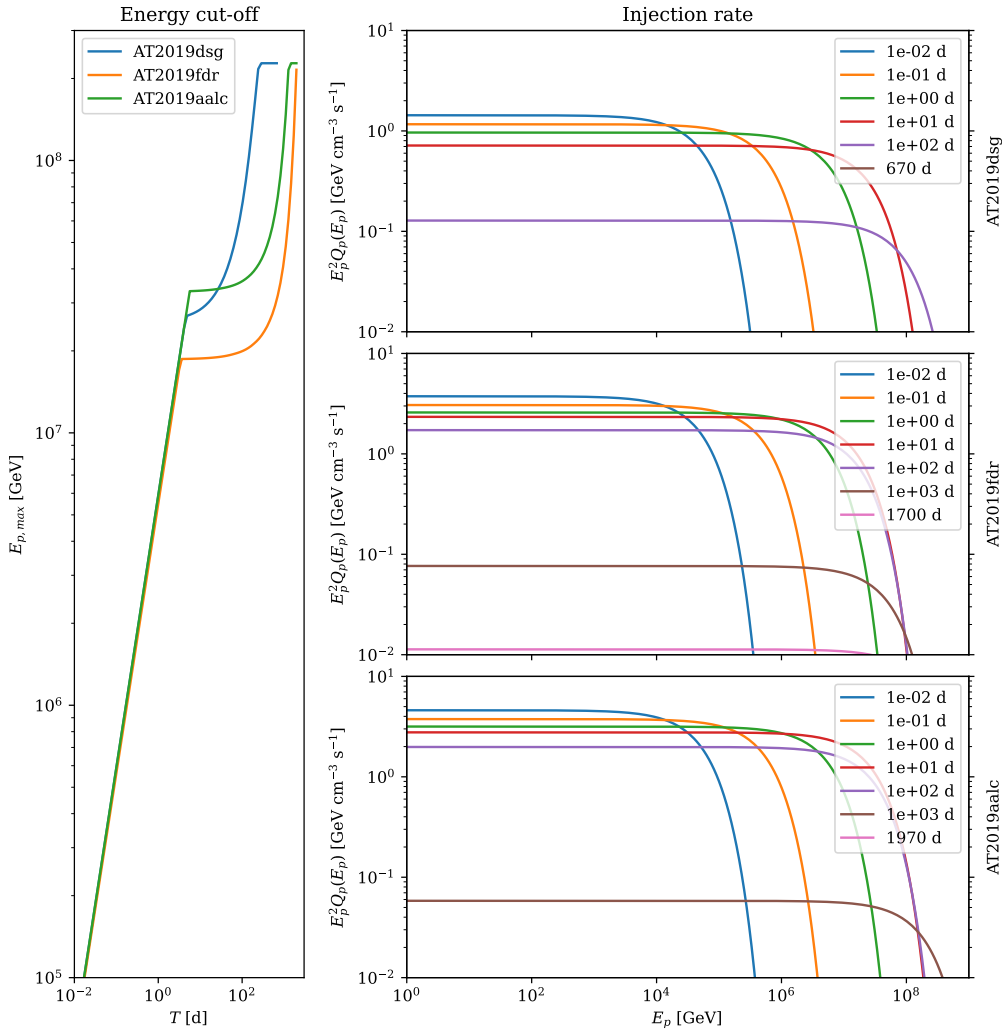

Figure 4.2.: Left: evolution of the cut-off in the proton injection spectrum over t_{dyn} for the three sources. Right: proton injection spectrum $Q_{\text{p}}(t, E_{\text{p}})$ (3.7) at several instants during the lifetime of the TDEs.

The functional shape of $t_{\text{c,bh}}$ is qualitatively similar to $t_{\text{c,p}\gamma}$, but shifted towards lower E_{p} because it has a lower kinematic threshold and norm than photomeson production. At $E_{\text{p}} \sim 10^5$ GeV, it has a time-independent relative minimum, which corresponds to pair production from X-ray photons. This process could dominate the low end of the electron spectrum, but $t_{\text{c,bh}}(E_{\text{p}} \sim 10^5$

GeV) $\gg t_{\rm dyn}$, so the total energy density dissipated in low-energy electrons is likely very low. On the contrary, the time scale for pair production with the OUV background, which corresponds to the absolute minimum at $E_{\rm p} \sim 10^6$ GeV, is efficient enough to be dynamically relevant, although Bethe-Heitler interactions in this energy range might compete with photomeson production off X-rays.

4.1.2 Electron acceleration and efficiency of radiative losses

The DSA and escape time scales are the same for protons and electrons, because they only depend on the parameters that define the TDE environment. Unlike protons, however, electrons cool mainly via radiative losses and inverse Compton scattering: $\mathcal{P}_{\rm ic}$ (2.34), $\mathcal{P}_{\rm syn}$ (2.36) and $\mathcal{P}_{\rm brems}$ (2.40) scale with $\sigma_{\rm T}$, which is suppressed by a factor $m_{\rm e}^2/m_{\rm p}^2$ in the case of protons.

Figure 4.3 shows that electron DSA is limited by very fast synchrotron losses in a magnetic field $B \sim 1$ G. Klein-Nishina corrections reduce the efficiency of inverse Compton cooling at $E_{\rm e} \gtrsim 10^3$ GeV, so the cut-off in AT2019dsg and AT2019aalc is set by $t_{\rm c,syn}$ at all times. As a result, its value plateaus after $t \sim 10^2$ s.

Inverse Compton scattering only competes with the acceleration time in AT2019fdr, where $t_{\rm c,ic} \sim t_{\rm syn}$ for $t \lesssim 600$ d and $E_{\rm e} \sim \mathcal{O}(10^3)$ GeV. This occurs because the OUV background in the source is an order of magnitude brighter than the others.

Bremsstrahlung and Coulomb-drag losses are subdominant in all cases, although some contribution to the electromagnetic spectrum from bremsstrahlung photons could be possible early on, when matter density is near its peak.

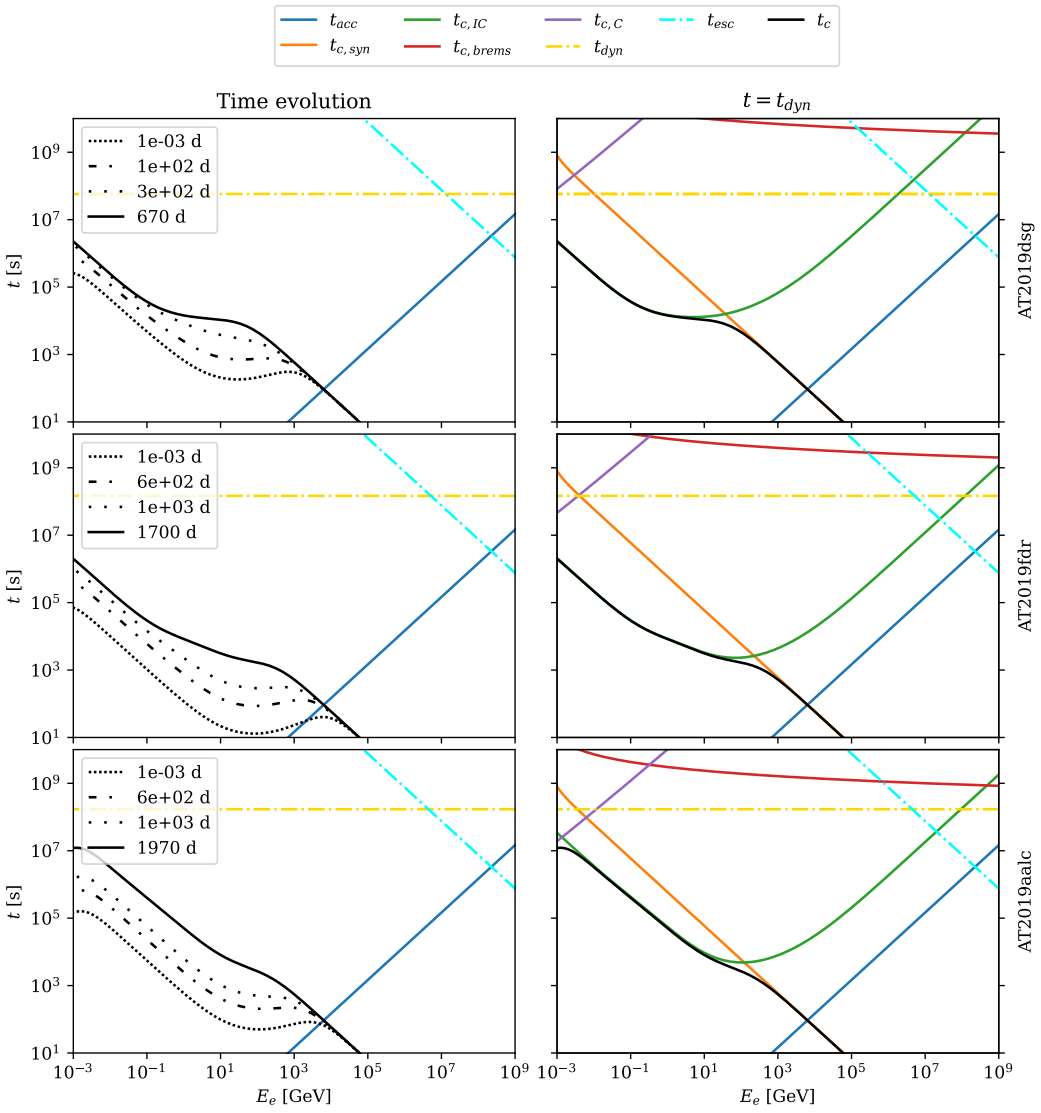

Figure 4.3.: Left: effective cooling time scale over the lifetime (t_{dyn}, golden dash-dotted) of the sources, compared with the DSA time scale (t_{acc}, dark blue) and the escape time (t_{esc}, cyan dash-dotted). Right: Individual cooling time scales at $t = t_{\mathrm{dyn}}$. The Coulomb time scale $t_{\mathrm{c,C}}$ in a fully ionized plasma is taken from [47] and plotted for completeness.

4.2 Proton and electron spectra

4.2.1 Proton spectrum

The proton injection rate Q_{p} (3.7) was plotted in Figure 4.2 for the three sources. The cut-off is set at every instant via (3.8) according to the results in

Section 4.1.1, and the normalization is determined via (3.11). As time passes and the target backgrounds fade, the rate extends to higher energies, but the overall injected energy density decreases because $\dot{M}(t)$ slows down.

The evolution of the proton spectrum was calculated using (2.45) and the results are shown in Figure 4.4. At $E_\mathrm{p} < 10^6$ GeV, $E_\mathrm{p}^2 n_\mathrm{p}(t, E_\mathrm{p})$ is flat. Cooling in this energy range is very inefficient, because it is dominated by inelastic pp collisions. Hence, the shape of the spectrum is set by DSA, $n_\mathrm{p} \propto E_\mathrm{p}^{-2}$, and the continuous injection of particles into the radiation zone just leads to an overall increase in the normalization of the density.

At $E_\mathrm{p} \gtrsim 10^6$ GeV, injection competes with faster cooling. The inequality $t < t_\mathrm{c}$ holds for the first few days, so energy losses are negligible and the spectrum traces Q_p. Afterwards, $E_\mathrm{p,max}$ increases slowly for $t \sim \mathcal{O}(10)$ d (Figure 4.2), which, along with fast cooling above the cut-off, leads to the formation of a small bump around $E_\mathrm{p} \sim 10^7$ GeV. Continuous energy losses over t_dyn slowly shift this bump towards the low end of the spectrum, most noticeably in the source with the highest OUV luminosity (AT2019fdr).

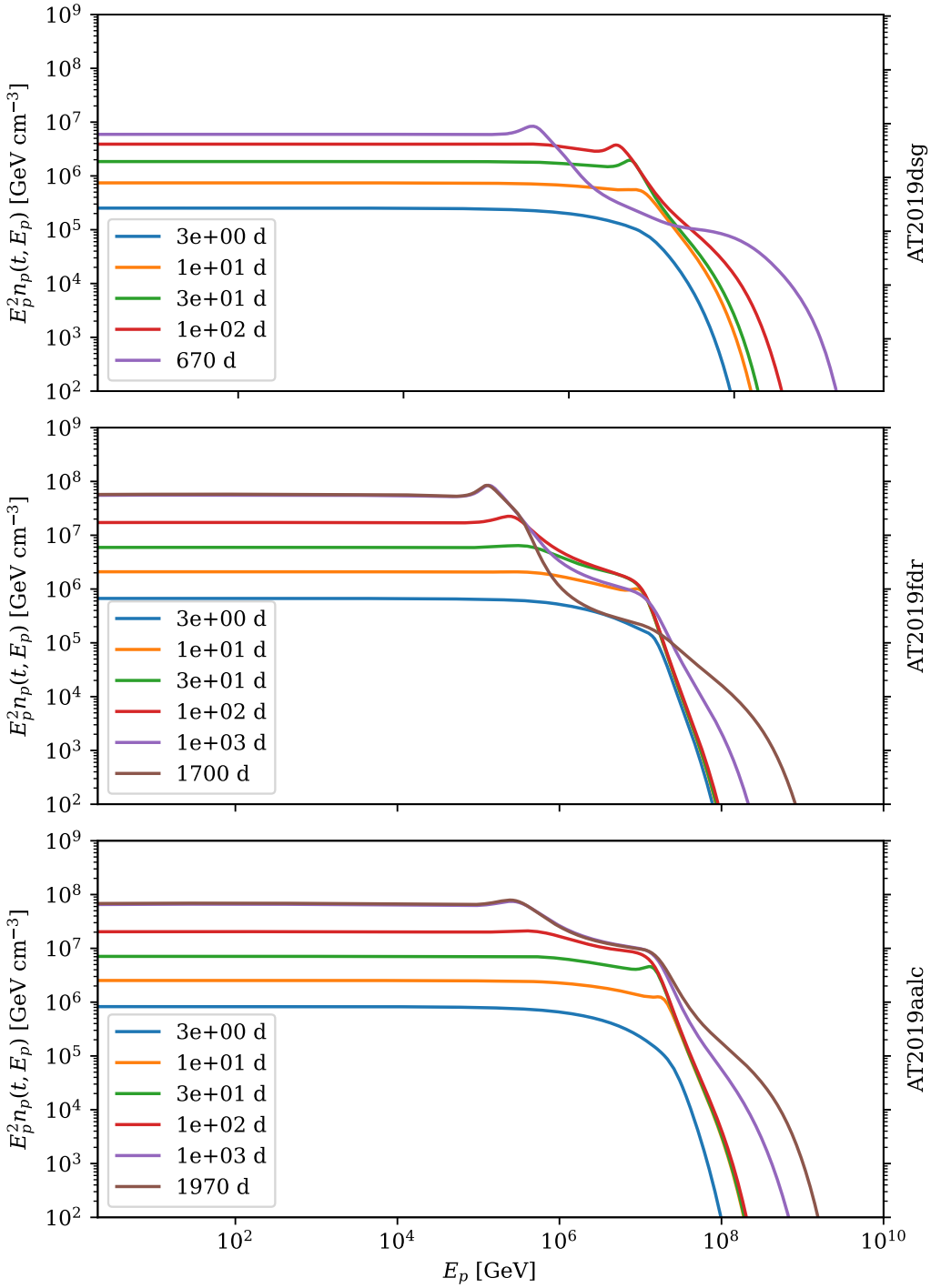

Figure 4.4.: Proton spectrum at different times during the events.

4.2.2 Electron spectrum

The in-source electron distribution has more distinctive features than the proton spectrum: it contains secondary electrons produced in (photo)hadronic

interactions, whose contributions to the overall spectrum have distinct shapes and peak in different energy ranges, and results from cooling time scales orders of magnitude shorter.

The spectral electron-positron injection rate is shown in Figure 4.5. At low energies $E_\mathrm{e} \lesssim 10^{-1}$ GeV, it is dominated by primary electrons with a power-law distribution ($Q_\mathrm{e;nt}$) from DSA. The normalization of $Q_\mathrm{e;nt}(t)$ decreases over time following the luminosity of the source, and its cut-off ($E_\mathrm{e,max} \sim \mathcal{O}(10^3)$ GeV) varies little over time, because it is set by $t_\mathrm{c,syn}$ for most of the dynamical time.

In the range 10^{-1} GeV $\lesssim E_\mathrm{e} \lesssim 10^4$ GeV, the energy density is dominated instead by secondary electrons from inelastic pp collisions ($Q_\mathrm{e;pp}$) and Bethe-Heitler pair production ($Q_\mathrm{e;bh}$). $Q_\mathrm{e;pp}$ extends towards lower energies than $Q_\mathrm{e;bh}$, because hadronic interactions are possible below the kinematic threshold for Bethe-Heitler cooling with X-rays ($E_\mathrm{p} \lesssim 10^3$ GeV, Figure 4.1). However, it is subdominant in all sources except AT2019aalc, where low X-ray luminosity and OUV background temperature lead to a small and relatively narrow Bethe-Heitler injection term. In this source, two peaks in $Q_\mathrm{e;bh}$ are clearly visible, which correspond to the interaction with X-rays ($E_\mathrm{e} \sim \mathcal{O}(1)$ GeV) and OUV targets.

These differences in the backgrounds also affect the contributions from photomeson production ($Q_{\mathrm{e};\mathrm{p}\gamma}$). These span the energy range 10^3 GeV $\lesssim E_\mathrm{e} \lesssim 10^8$ GeV, and peak around $E_\mathrm{e} \sim 10^5$ GeV: secondary electrons originated in photohadronic interactions do not undergo DSA, so they are not affected by the cut-off imposed by synchrotron cooling on primary electrons. Around the peak, the height of $Q_{\mathrm{e};\mathrm{p}\gamma}$ is a factor ~ 2 lower than in the other two sources, because the spectral distribution and overall normalization of the target backgrounds leads to comparatively inefficient interactions with high-energy protons.

On the contrary, above $E_\mathrm{e} \gtrsim 10^7$ GeV these terms look very similar. Since the typical inelasticity of photomeson production is $K_{p\gamma} \sim 0.2$ (Section 2.3), these electrons likely result from interactions of protons with $E_\mathrm{p} \sim 0.1$ EeV. This corresponds to the cut-off in the CR spectrum (Figures 4.2 and 4.4), so $Q_{\mathrm{e};\mathrm{p}\gamma}$ is also exponentially suppressed at high energies.

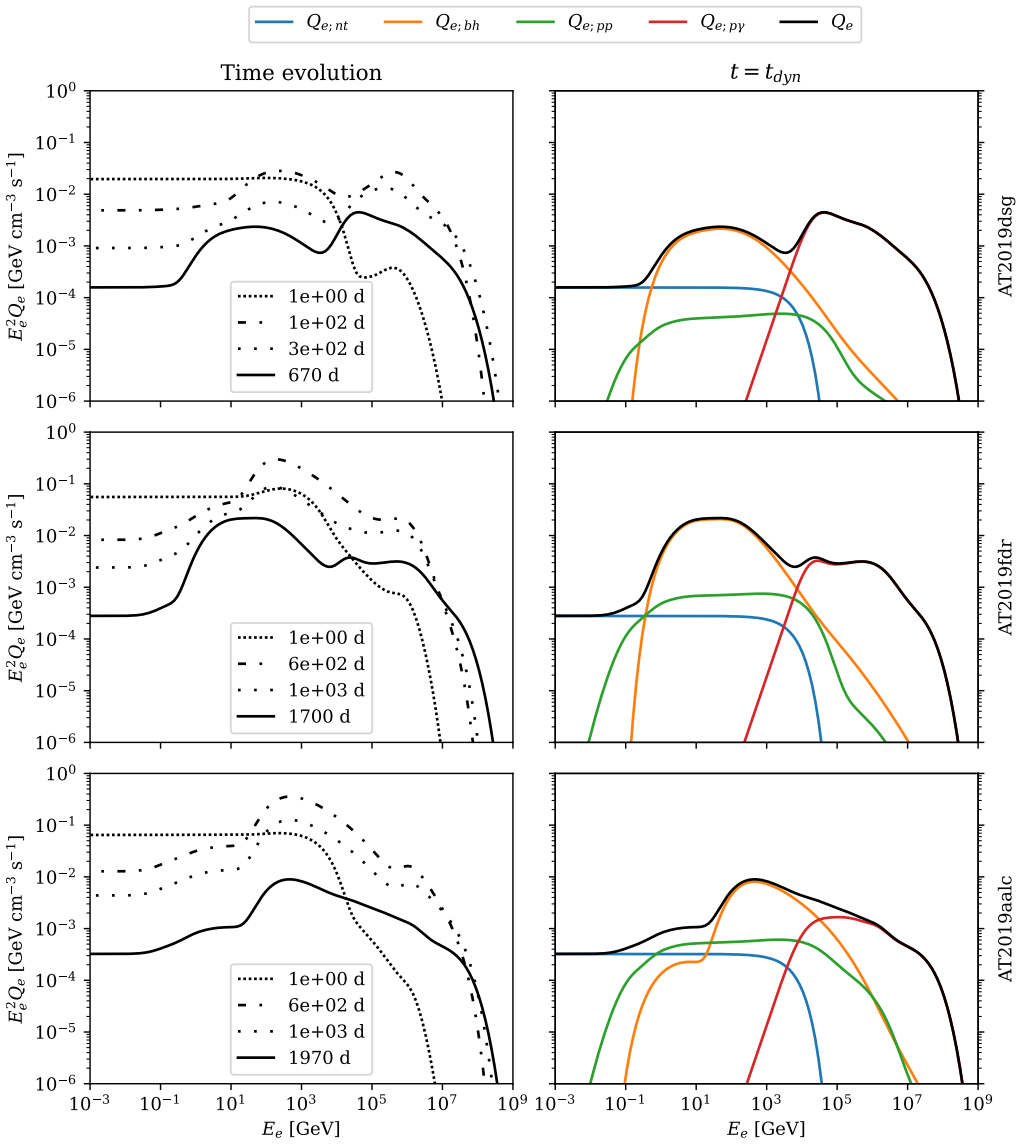

Figure 4.5.: Spectral injection rate of charged leptons in the three TDEs. Left: total rate Q_e over time. Right: rate at $t = t_\mathrm{dyn}$ as a sum of electrons from DSA ($Q_\mathrm{e;nt}$), Bethe-Heitler pair production ($Q_\mathrm{e;bh}$), inelastic pp scattering ($Q_\mathrm{e;pp}$) and photomeson production ($Q_\mathrm{e;p\gamma}$)

Figure 4.6 shows the evolution of the electron spectrum $n_\mathrm{e}(t, E_\mathrm{e})$ over the lifetime of the TDEs. A local minimum is formed around $E_\mathrm{e} \sim \mathcal{O}(10)$ GeV over the first few hours ($\partial(E_\mathrm{e}^2 n_\mathrm{e})/\partial E_\mathrm{e} = 0$): this is caused by IC cooling. At these energies, synchrotron emission is subdominant, so $t_\mathrm{c} \sim t_\mathrm{c,ic}$, which also has a local minimum due to the transition from the Compton to the Klein-Nishina regime ($\partial t_\mathrm{c}^{-1}/\partial E_\mathrm{e} \simeq 0$). Moreover, $n_\mathrm{e}(E_\mathrm{e} \sim 10^2$ GeV$)$ stays approximately

constant over $\mathcal{O}(10)$ d ($\partial n_\mathrm{e}/\partial t \simeq 0$). In these conditions, (2.45) reduces to $E_e^2 n_e(E_e, t) \simeq t_{\mathrm{c,ic}}(E_\mathrm{e}, t)[E_\mathrm{e}^2 Q_\mathrm{e}(E_\mathrm{e}, t)]$.

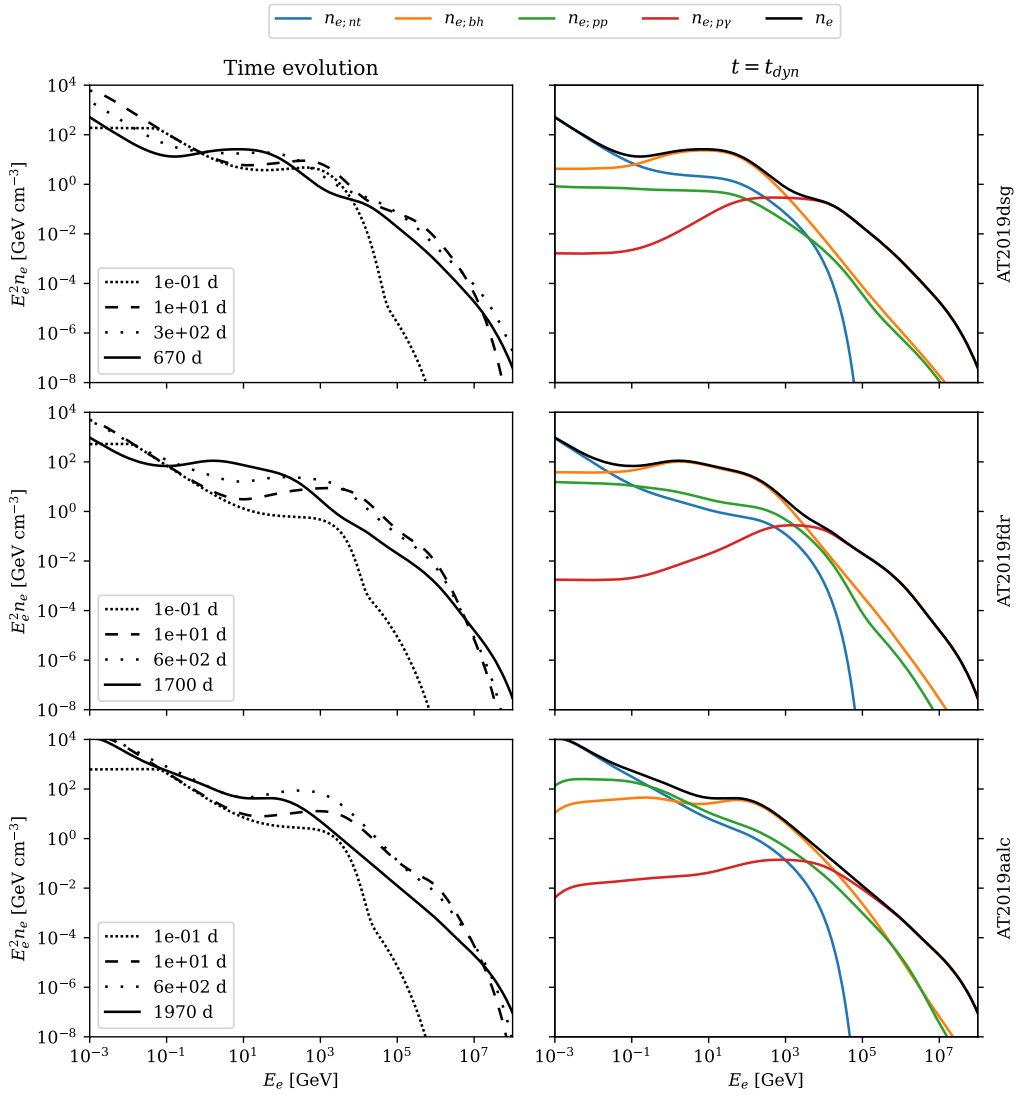

Figure 4.6.: In-source electron-positron density. Left: evolution of the overall energy density $E_\mathrm{e}^2 n_\mathrm{e}$ during the TDEs. Right: energy density at $t = t_\mathrm{dyn}$ as a sum of electrons from DSA ($n_\mathrm{e;nt}$), Bethe-Heitler pair production ($n_\mathrm{e;bh}$), inelastic pp scattering ($n_\mathrm{e;pp}$) and photomeson production ($n_\mathrm{e;p\gamma}$)

Early on, injection is dominated by primary electrons, which means $E_e^2 Q_e$ is energy-independent, because the relevant energy range is far below the cut-off. Hence, $E_\mathrm{e}^2 n_\mathrm{e}$ and $t_\mathrm{c,ic}$ have approximately the same functional form for a period of $\mathcal{O}(10)$ d. The electrons cooled via inverse Compton scattering cascade towards the low end of the spectrum, which causes a rapid increase in the energy density at $E_\mathrm{e} \lesssim 10$ GeV.

The shape of $n_{\rm e}$ at higher energies is determined by the competition between cooling and the injection of secondary electrons. The spectrum rapidly develops a local maximum at $E_{\rm e} \sim 10^4$ GeV, due to synchrotron losses above $E_{\rm e,max}$: this peak then shifts towards lower energies as synchrotron emission becomes dynamically relevant in an increasingly large energy range ($t > t_{\rm c,syn}$).

After a day, synchrotron cooling is expected to cause significant energy losses in the region of the spectrum dominated by inverse Compton scattering, because $t_{\rm c,syn}(E_{\rm e} \sim 10$ GeV$) \sim 10^5$ s (Figure 4.3). This, combined with the decreasing efficiency of the latter, flattens the relative minimum created during the first hours of the event. The injection of Bethe-Heitler pairs in this energy range then leads to another relative maximum in AT2019dsg and AT2019fdr. In AT2019aalc, this contribution peaks at higher energies and is comparatively smaller (Figure 4.5), the competition between injection and cooling results in a saddle point.

4.3 Multi-wavelength electromagnetic spectra of Tidal Disruption Events

4.3.1 Evidence of (photo)hadronic interactions in the infrared to X-ray range

Charged leptons are not feasible astronomical messengers in the study of extragalactic sources, because escape from the radiation zone occurs long before they can cool. However, the photons they emit while they are magnetically confined could potentially be observed. Radiation from the decay of mesons or the cooling of electrons produced in (photo)hadronic interactions is a probe for the population of protons in TDEs and could offer evidence that the latter are transient sources of high-energy neutrinos.

The fluence of radiation from charged leptons has been estimated as:

$$\mathcal{F}_\gamma(t, E_\gamma) = \sum_{i,j} \frac{R^3}{3 d_{\rm L}^2} \int_0^t dt' \int_{m_{\rm e}c^2}^\infty dE_{\rm e} n_{{\rm e};j}(t', E_{\rm e}) \mathcal{P}_i(t', E_{\rm e}, E_\gamma), \tag{4.2}$$

where $i =$ syn, brems, ic; $j =$ nt, bh, pp, pγ; and d_{L} is the luminosity distance of the TDE (Appendix B.1). The decay of unstable mesons from pp and pγ interactions into high-energy photons is also considered: in this case, the corresponding power $\mathcal{P}$ is calculated via (2.27).

In Figures 4.7 and 4.8, the integrated photon flux of the three sources is shown at $t = t_{\mathrm{dyn}}$ as a sum of contributions from different proton and electron cooling mechanisms. The former intends to highlight the energy ranges where observational studies of the electromagnetic spectrum could potentially find evidence of photohadronic interactions, e.g. in the hard X-rays; the latter clarifies which radiative processes give rise to the features in the spectrum.

The plasma outflow causes a low-energy cut-off in the synchrotron emission due to the Razin-Tsytovich effect (Appendix A.2), so the radio spectrum ($E_\gamma \lesssim 10^{-16}$ GeV) is suppressed. Microwaves (10^{-16} GeV$\lesssim E_\gamma \lesssim 10^{-13}$ GeV) are dominated by emissions from primary electrons (NT), mainly due to synchrotron radiation: integration over a broad range of E_{e} turns the characteristic shape of $\mathcal{P}_{\mathrm{syn}}$ into a power law, so the fluence plateaus at low energies. This effect is also noticeable in the subdominant contributions from Bethe-Heitler (BH), pp and photomeson (pp+pγ) electrons, although in this case the shape of the fluence is closer to the single-electron synchrotron spectrum, because $n_{\mathrm{e;bh}}$, $n_{\mathrm{e;pp}}$ and $n_{\mathrm{e;p}\gamma}$ are much lower than $n_{\mathrm{e;nt}}$ in the relevant energy range.

In the infrared (10^{-12} GeV $\lesssim E_\gamma \lesssim 10^{-10}$ GeV) to extreme ultraviolet ($E_\gamma \sim 10^{-7}$ GeV), the NT and BH contributions are comparable. TDE surveys could potentially obtain some indication of photohadronic interactions via fits of the electromagnetic spectrum in this energy range: OUV emissions by primary electrons mainly correspond to background photons upscattered via IC collisions, whereas Bethe-Heitler emissions are still synchrotron-dominated.

From an observational point of view, the most relevant result is that the dominant contributions to the X- (10^{-7} GeV $\lesssim E_\gamma \lesssim 10^{-3}$ GeV) and γ-ray (10^{-3} GeV $\lesssim E_\gamma \lesssim 10^{2}$ GeV) spectra come from secondary particles of Bethe-Heitler and neutrino-producing interactions.

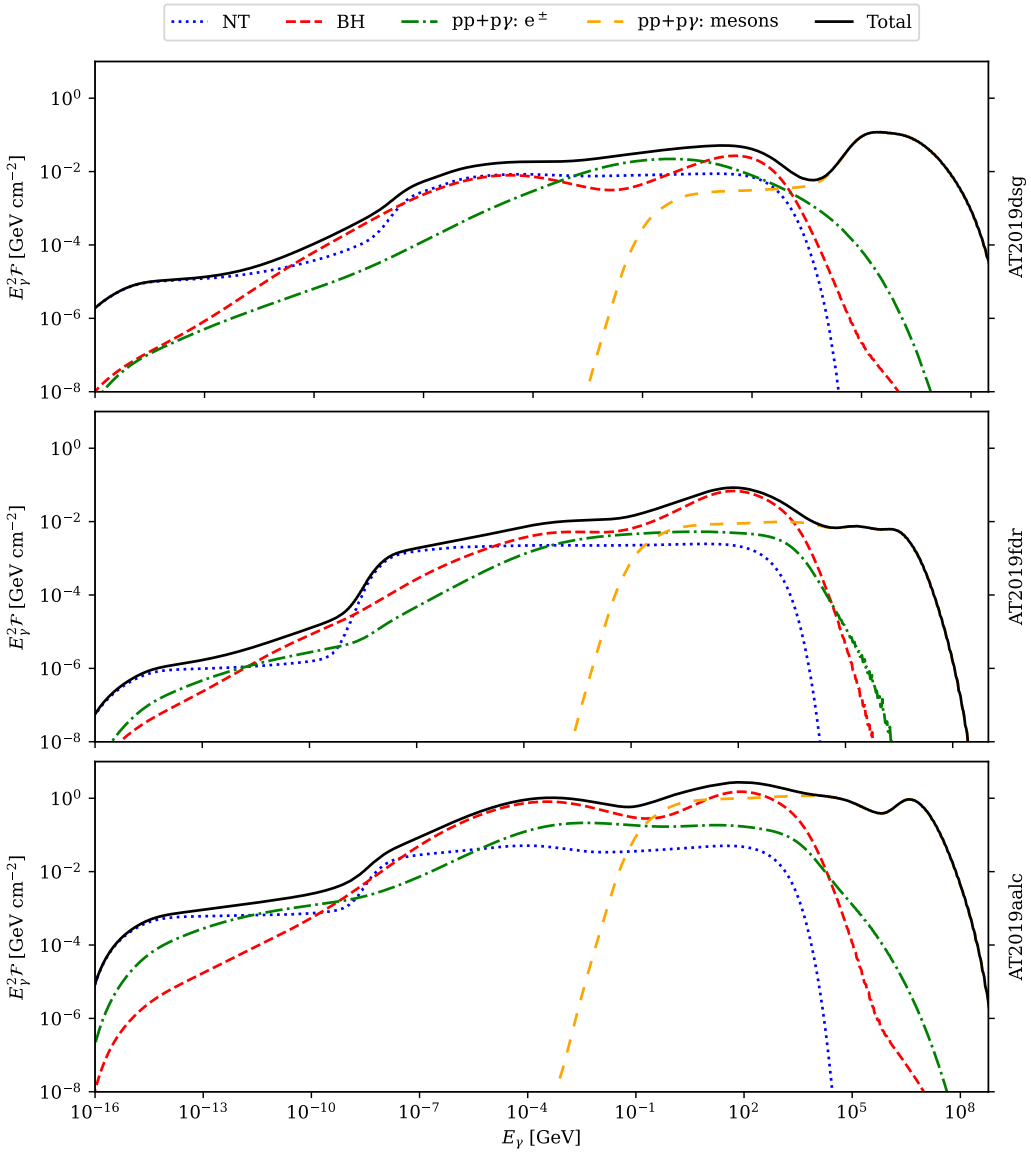

Figure 4.7.: Photon fluence from meson disintegration, and from the cooling of primary (NT), Bethe-Heitler (BH), proton-proton and photomeson (pp+pγ) electrons.

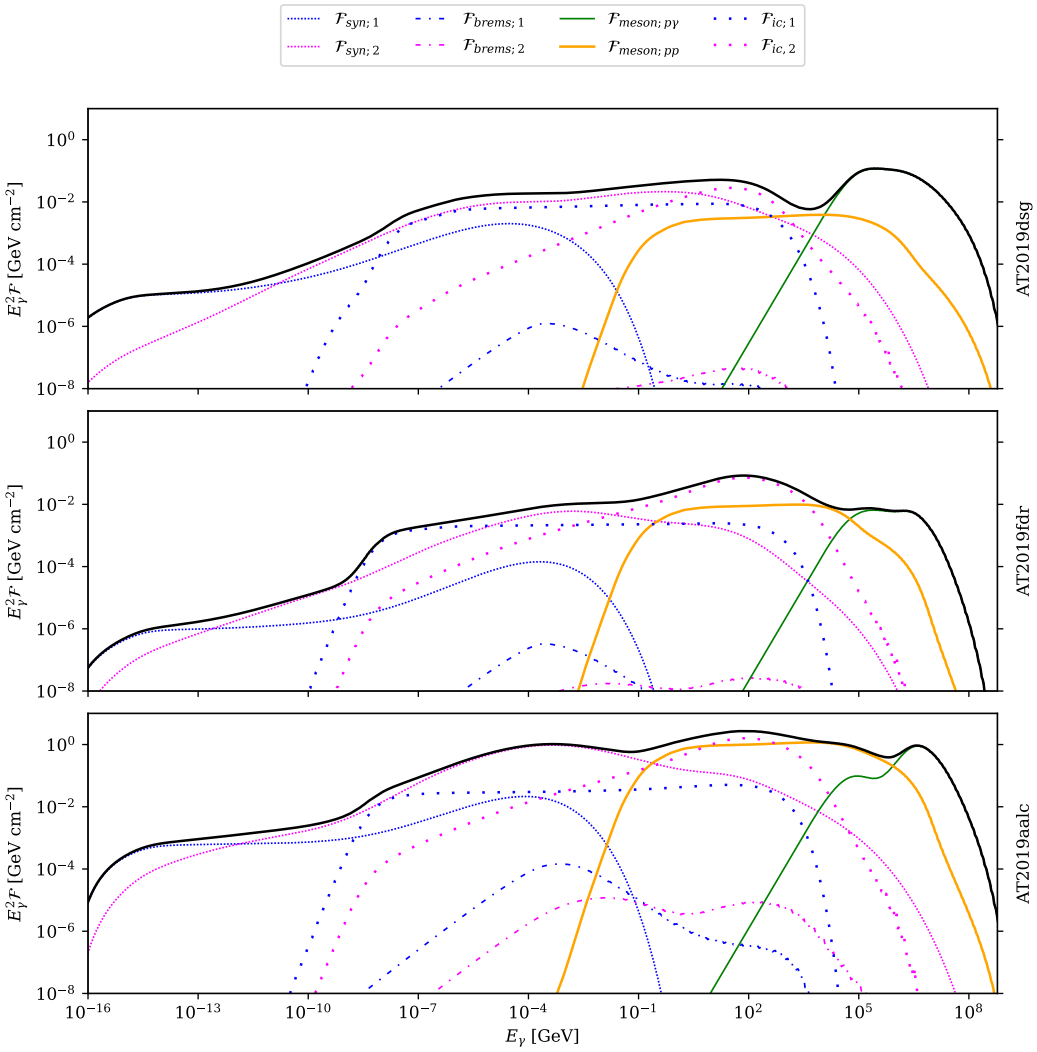

Figure 4.8.: Photon fluence as a sum of contributions from different electron cooling processes and meson disintegration. Subindex 1 refers to primary electrons; subindex 2 refers to secondary electrons from Bethe-Heitler, pp and pγ interactions.

The pp+pγ spectrum in the X-rays resembles the single-electron synchrotron spectrum, but becomes flatter in the γ-rays due to IC scattering. In comparison, the shape of the BH spectrum in this energy range shows a characteristic „double hump“, which results from synchrotron emission in the X-rays and upscattered IC photons in the γ-rays. However, synchrotron emission is still significant at high energies and dominates the very-high-energy γ-ray emission ($E_\gamma \gtrsim 10^2$ GeV) from BH electrons in AT2019dsg and AT2019fdr. This is due to the cooling of electrons injected at $E_\mathrm{e} \gtrsim 10^5$ GeV ($\gamma_\mathrm{e} \sim 10^7 - 10^8$), which radiate at a typical synchrotron frequency $\hbar\omega_\mathrm{c} \sim 10^{-2}$ GeV. On the contrary, the synchrotron component of the AT2019aalc is subdominant at high energies,

which may be due to pp collisions being more efficient than photohadronic cooling in this source.

4.3.2 γ-ray opacity and absorption in the extragalactic medium

The strongest evidence of neutrino production that could be obtained from the electromagnetic spectrum would be the detection of γ-rays from the decay of π^0 and η mesons produced in pp and pγ interactions. The contribution from pp mesons is comparable to the BH curve in AT2019aalc, where radiation backgrounds are faint and photohadronic cooling is relatively inefficient; photopion decay dominates the very-high-energy γ-ray band ($E_\gamma \gtrsim 10^2$ GeV) of the three sources.

Detecting these particles is highly unlikely due to $\gamma\gamma$ absorption in the source and en route to Earth. Indeed, very-high-energy photons are absorbed over length scales much shorter than d_L by an extragalactic background of photons accumulated star formation and emissions by active galactic nuclei [63]. This leads to an exponential suppression of the spectrum ($\mathcal{F}_\mathrm{Earth}$) by a redshift- ($z$) and energy-dependent coefficient:

$$\mathcal{F}_\mathrm{Earth}(z, E_\gamma) = \mathcal{F}(E_\gamma) e^{-\kappa(z, E_\gamma)}. \tag{4.3}$$

Figure 4.9 shows the effect of γ-ray absorption on the total fluences, interpolating the values of κ from [64] in the redshift range $0.01 \leq z \leq 0.3$.

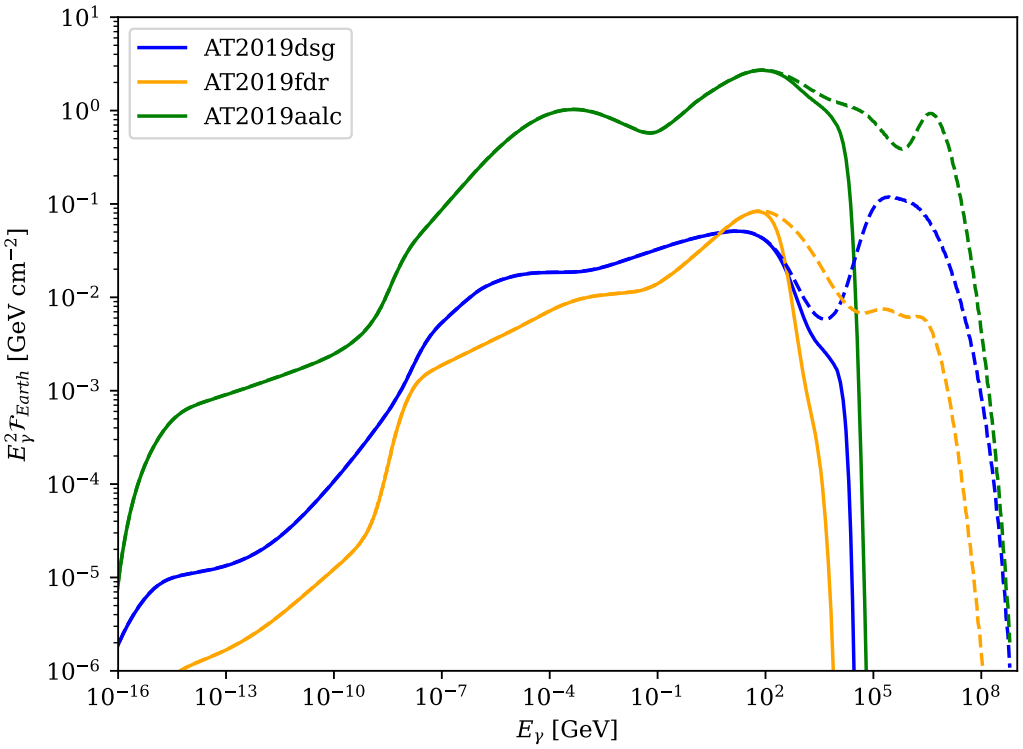

Figure 4.9.: Effect of γ-ray absorption in the extragalactic background light at $t = t_{\rm dyn}$. Dashed lines represent unabsorbed fluences.

γ-rays with energies $E_\gamma \sim \mathcal{O}(100)$ GeV are also possibly absorbed in the thermal OUV background of the sources:

$$\gamma + \gamma_{\rm ouv} \rightarrow {\rm e}^- + {\rm e}^+. \tag{4.4}$$

A detailed treatment of this process is outside the scope of the thesis, because it starts an electromagnetic cascade that reprocesses the energy of the primary γ-ray into lower energies. However, its importance can be estimated by calculating the following optical depth [65]:

$$\tau_{\gamma\gamma}(E_\gamma, t) = \int_0^R dr \int d\Omega (1-\cos\theta) \int_{\frac{2m_{\rm e}^2c^4}{E_\gamma(1-\cos\theta)}}^{\infty} d\epsilon \rho(\mathbf{r}, \epsilon, t) \sigma_{\gamma\gamma}(E_\gamma, \epsilon, \cos\theta), \tag{4.5a}$$

$$\sigma_{\gamma\gamma}(\beta) = \frac{3\sigma_{\rm T}}{16}(1-\beta^2)\left[2\beta(\beta^2-2) + (3-\beta^4)\ln\left(\frac{1+\beta}{1-\beta}\right)\right], \tag{4.5b}$$

$$\beta(E_\gamma, \epsilon, \cos\theta) = \sqrt{1 - \frac{2m_{\rm e}^2c^4}{E_\gamma\epsilon(1-\cos\theta)}}, \tag{4.5c}$$

where the integration limits follow from kinematic cuts. The result can be written as the ratio $\tau_{\gamma\gamma} = t_{\rm fs}/t_{\gamma\gamma}$ of the free streaming time to the interaction time scale $t_{\gamma\gamma}$ when the backgrounds are homogeneous.

Figure 4.10 shows the optical depth for each of the TDEs $\mathcal{O}(100)$ d into the super-Eddington phase. 2-photon pair production is more efficient in the presence of very-low-energy radiation, so $\tau_{\gamma\gamma}$ is larger in the sources with colder backgrounds. In particular, the process is highly suppressed for AT2019aalc in the energy range 10^{-1} GeV $< E_\gamma < 10^{1}$ GeV because the X-ray temperature is 100 eV higher than in the other TDEs (Appendix B.1).

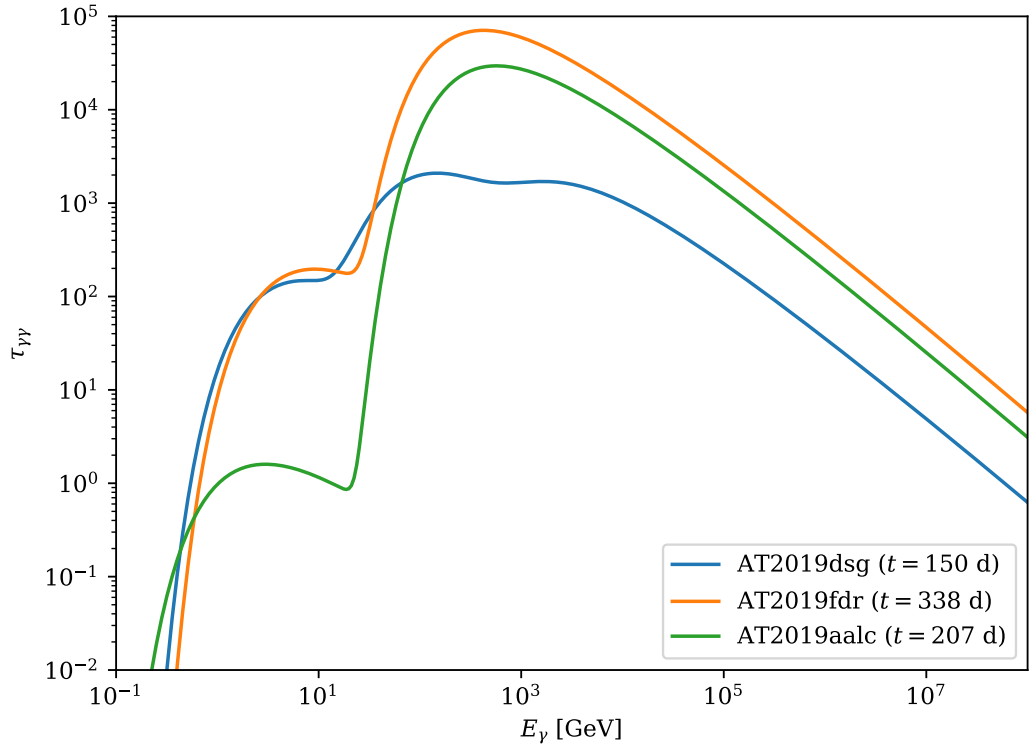

Figure 4.10.: Optical depth of 2-photon pair production as a function of γ-ray energy. The chosen times correspond to the end of the Fermi-LAT observation period of the sources [9].

Regardless, for $\tau_{\gamma\gamma} \gg 1$, the effect on the fluence can be modelled via:

$$\mathcal{F}_{\rm observed} \sim \frac{1 - e^{-\tau_{\gamma\gamma}}}{\tau_{\gamma\gamma}} \mathcal{F} \sim \frac{\mathcal{F}}{\tau_{\gamma\gamma}}. \tag{4.6}$$

which means the fluence is suppressed by a factor $\tau_{\gamma\gamma}^{-1} \sim 10^{-2} - 10^{-4}$ at 10 GeV $< E_\gamma <$ 100 GeV. The energy of these γ-rays is reprocessed through an

electromagnetic cascades down to the energy range where absorption becomes inefficient ($\tau_{\gamma\gamma} \sim 1$), which Figure 4.10 shows to be $\mathcal{O}(100)$ MeV to $\mathcal{O}(1)$ GeV depending on the source.

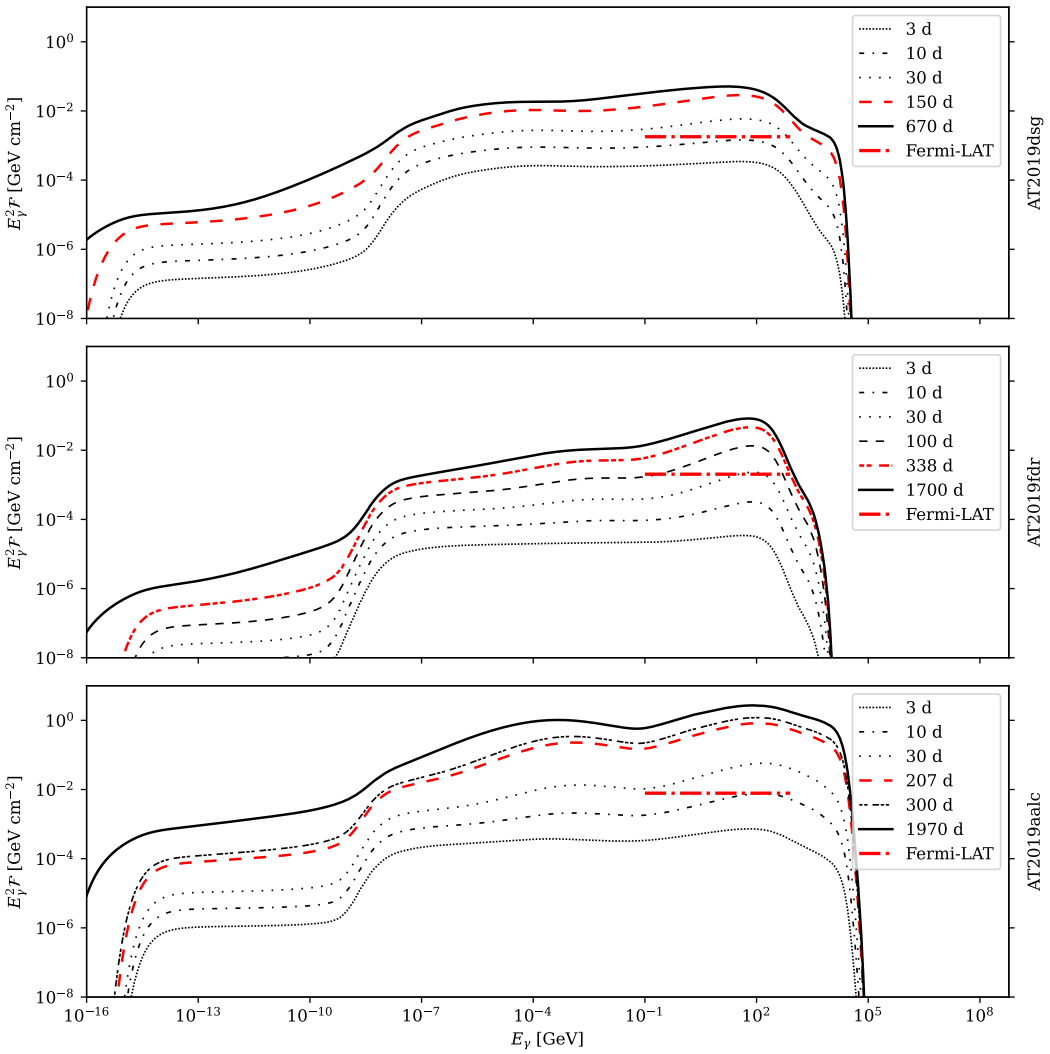

Figure 4.11.: Time evolution of the photon fluence, compared with the 95% confidence-level Fermi-LAT upper limit at $t = 150$ d (AT2019dsg), $t = 338$ d (AT2019fdr) and $t = 207$ d (AT2019aalc) [9].

This could explain why the photon fluxes in this work are in tension with the non-detection of γ-rays by the Fermi-LAT telescope [9]. Observations of the sources in the 0.1 GeV $< E_\gamma <$ 800 GeV energy range placed an upper bound on their fluences at $E_\gamma^2 \mathcal{F} \sim 10^{-2}$ GeV in $\mathcal{O}(100)$ d. Figure 4.11 shows that IC emissions from Bethe-Heitler pairs exceed this limit by a factor ~ 10 (AT2019dsg, AT2019fdr) or $\sim$ 100 (AT2019aalc). Part of this discrepancy could be absorbed into any of the free parameters in the model, particularly

because the fiducial efficiency of CR acceleration is unusually high (Appendix B.1). However, overproduction of photons by orders of magnitude points to significant absorption by the OUV background. High X-ray and soft γ-ray luminosity could thus be evidence of the presence of high-energy protons and photohadronic interactions in TDEs, as the energy in the primary γ-rays would get reprocessed into 100 MeV photons.

4.4 Neutrino fluences on Earth

The flavour-averaged neutrino fluence ($\mathcal{F}$) on Earth from each of the TDEs is shown in Figure 4.12. The time-integrated flux falls below the IceCube Gamma-ray Follow-Up (GFU) differential limit for all sources except AT2019aalc [18], where low X-ray background luminosities lead to a significant production of neutrinos in pp interactions and photomeson production off the OUV targets. However, the average energy of the distributions lies in the correct energy range of 100 TeV and is consistent with observations [10, 11].

At low energies, the spectrum is dominated by pp neutrinos. Since the scattering target in TDEs is cold gas, the fluence traces the spectrum of high-energy protons: an E_ν^{-2} power-law with an exponential cut-off ($E_\nu \sim 10^4$ GeV). The normalization of this contribution exceeds the value in the M-X model of [18] by a factor ~ 5, which is the ratio between the outflow velocities assumed in both works. Furthermore, the cut-off in the spectrum is located towards higher energies, due to $E_{\mathrm{p,max}}(t)$ reaching higher values in the EeV range at the end of the TDE. It is shown in Appendix C that the results in the literature are reproduced when the same benchmark values of v_{out} and $E_{\mathrm{p,max}}$ are used.

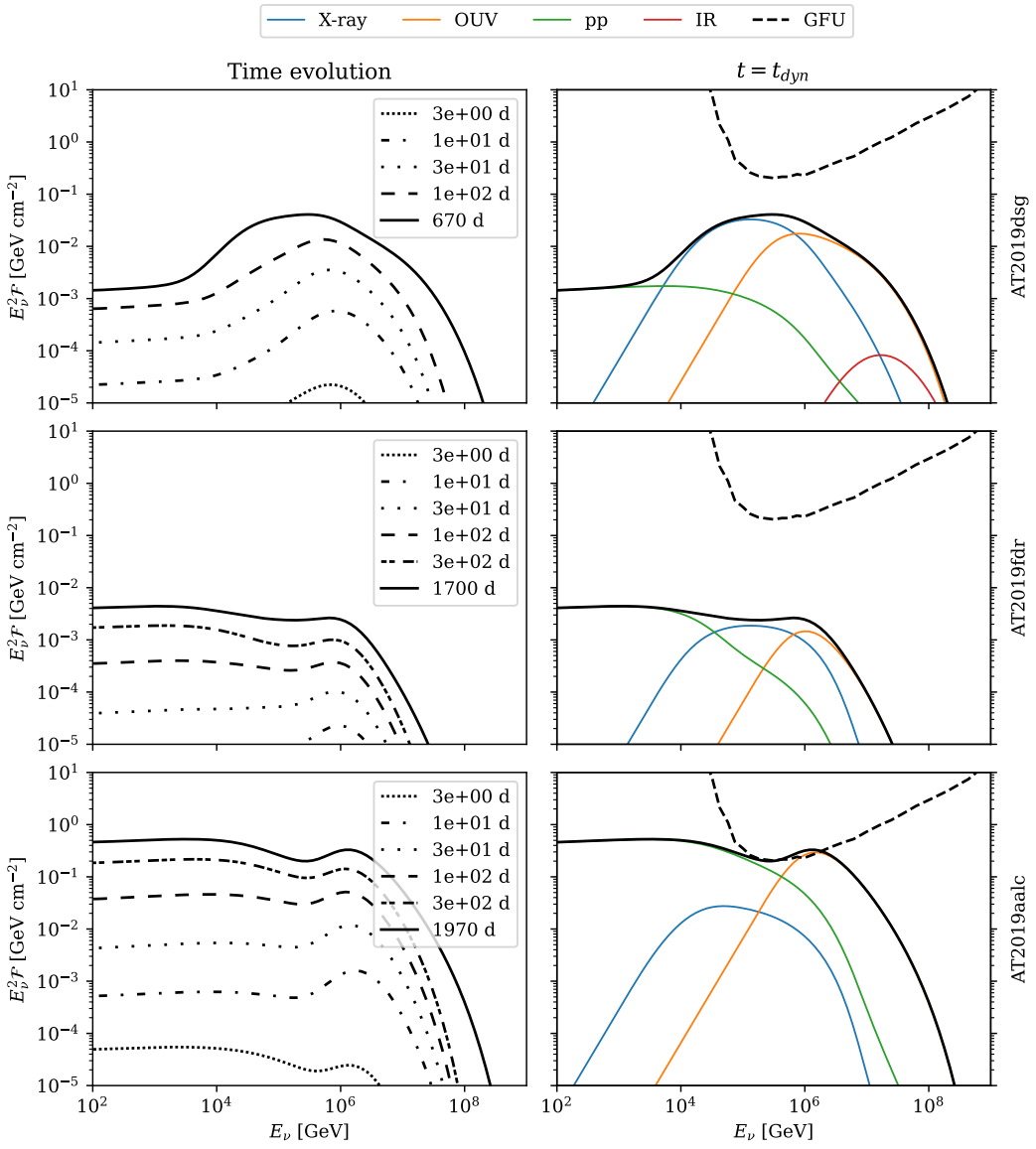

Figure 4.12.: Flavour-averaged neutrino fluences on Earth. Left: time evolution of the total fluence. Right: fluence at $t = t_{\mathrm{dyn}}$ as a sum of contributions from different CR cooling mechanisms.

Photomeson production off OUV backgrounds is suppressed by the exponential cut-off in the primary CR spectra. Neutrino fluences from these interactions are peaked around a typical energy (3.1), which in the case of OUV photons requires proton energies that can not be achieved efficiently over the lifetime of the transients. Hence, very high target densities are needed in order to achieve significant neutrino fluxes. The OUV target in AT2019fdr has 100 times the luminosity of the X-rays, so photomeson production off both targets leads to similar neutrino energy densities. On the contrary, AT2019dsg is much

more faint in the OUV band, so the bulk of neutrino production comes from the interaction with X-rays.

The results in AT2019aalc are somewhat more complex: its OUV luminosity is comparable to AT2019dsg, but the neutrino fluence is much higher. It is possible that the low X-ray luminosity of AT2019aalc allows for very efficient interactions between very-high-energy CRs and the OUV background. This is supported by [18]: the shape of the fluence closely resembles the results obtained in the M-OUV model in that paper, which allows for photomeson production from EeV CRs.

Finally, interactions with an IR dust echo only lead to significant neutrino production in AT2019dsg. This result mainly stems from the relative sizes of the radiation zone and the dust torus, which is 10 times larger in this source, but 50 times larger in AT2019fdr and AT2019aalc. Fainter IR backgrounds along with extremely high CR energy requirements lead to negligible neutrino production in the latter two sources.

The GFU effective area $A_{\text{eff}}(E_\nu)$ is taken from [66] and plotted as $\mathcal{F}_{\text{gfu}} \equiv E_\nu / A_{\text{eff}}(E_\nu)$ to illustrate the perspectives on the detection of neutrinos from these sources. The expectation value of IceCube events caused by a certain source can be written as:

$$\langle N_\nu \rangle = \int dE_\nu \mathcal{F}(E_\nu) A_{\text{eff}}(E_\nu), \tag{4.7}$$

so $\mathcal{F}_{\text{gfu}}$ roughly represents the energy flux required to trigger the Gamma-Ray Follow-up assuming that the emitted neutrino fluence is constant over an energy interval dE_ν. Said Follow-up is a real-time alert system: when high-energy events are detected, known γ-ray sources in the corresponding region of the sky are scanned to look for electromagnetic counterparts. The predicted fluences imply that neutrino emissions from TDEs are unlikely to be associated with electromagnetic flares from said sources in real time. Rather, TDEs could be established as point sources of astrophysical neutrinos in long-term surveys of IceCube data [18].

Conclusions and outlook

5

The main goal of this project was to predict the emission of neutrinos from TDEs in a self-consistent model, improving where possible on [18].

The most notable technical refinement with respect to that work has been the estimation of the cut-off in the primary proton spectrum from the balance between the cooling and acceleration time scales in the radiation zone. Under the assumption of Bohm-like diffusive shock acceleration, it has been found that protons in the disrupted stellar material may reach PeV energies or higher in a time scale of a few days, which is enough for the production of 100 TeV neutrinos. This result is robust to uncertainties in the disruption, fallback and accretion processes, since first-order Fermi acceleration takes place on time scales significantly shorter than these processes for reasonable values of the relevant parameters.

Secondly, this thesis expands on the literature by calculating the in-source density of charged leptons and the electromagnetic spectra of the TDEs. The results predict that the X-ray energy range should be dominated by synchrotron radiation and photons upscattered via inverse Compton collisions off secondary electrons from photohadronic interactions. Furthermore, a discussion of γ-ray absorption in the radiation zone has led to suggest that photopion decay could lead to a significant contribution in this band if the energy is reprocessed through an electromagnetic cascade. Therefore, high luminosities in this region of the spectrum could be evidence that high-energy CRs are accelerated and undergo neutrino-producing interactions in TDEs.

Finally, the neutrino fluences on Earth have been calculated using analytical estimates of the pp collision and photopion production cross sections. The overall normalization of the fluxes fall below the GFU differential limit. Detection of TDE neutrinos with IceCube is possible because this Observatory can register events from a broad population of sources spread throughout the Universe: even if the expectation value of events from each individual source is low, the whole population might add up to a number of events larger than 1.

However, real-time detection of neutrinos from specific TDEs likely requires a new generation of more sensitive neutrino observatories. The average energy of the distribution is consistent with observations and the relation between the spectrum of primary protons, the scattering backgrounds and the shape of the neutrino spectrum is well understood.

From a technical standpoint, the main limitation of this work has been the use of Python to calculate the spectra of electrons and primary protons in the sources. This has made it impossible to treat phenomena such as photomeson production off synchrotron photons, synchrotron self-Compton emission, or electromagnetic cascades. A more refined numerical framework is required in order to deal with non-linear effects that might have a significant effect on the results. Specifically, the possibility that synchrotron self-Compton might compete with γ-ray absorption in the source AT2019aalc could lead to significant corrections to the electromagnetic spectrum obtained in this work (Appendix C).

Furthermore, the fluences presented in this work offer the possibility of estimating the diffuse neutrino emission from TDEs. This result would be mainly susceptible to the cosmological rate of TDEs, which has been studied e.g. in [7, 24] as a way to probe the $M_\bullet - \sigma$ relation for SMBHs. This line of research would not only constrain the parameter space of possible sources of the neutrino background, but also offer an insight into structure formation in the early stages of the Universe.

A Technical implementation of cooling mechanisms

A.1 Bethe-Heitler cross section

The differential cross-section for Bethe-Heitler pair production is given by [45]:

$$\begin{aligned}\frac{d\sigma}{d\epsilon_- d\cos\theta_-} &= \frac{\alpha Z^2 r_0^2 p_- p_+}{2\epsilon^3}\left[-4\sin^2\theta_-\frac{2\epsilon_-^2+1}{p_-^2\Delta_-^4}+\frac{4\epsilon_-^2-2\epsilon_+\epsilon_-+3}{p_-^2\Delta_-^2}+\frac{p_-^2-\epsilon^2}{T^2\Delta_-^2}\right.\\ &+\frac{2\epsilon_+}{p_-^2\Delta_-}+\frac{Y}{p_-p_+}\times\left(2\epsilon_-\sin^2\theta_-\frac{3\epsilon+p_-^2\epsilon_+}{\Delta_-^4}+\frac{2\epsilon_-^2(\epsilon_-^2+\epsilon_+^2)}{\Delta_-^2}\right.\\ &\left.-\frac{7\epsilon_-^2+3\epsilon_+\epsilon_-+\epsilon_+^2-1}{\Delta_-^2}+\frac{\epsilon(\epsilon_-^2-\epsilon_-\epsilon_+-1)}{\Delta_-}\right)\\ &\left.-\frac{\delta_+^T}{p_+T}\left(\frac{2}{\Delta_-^2}-\frac{3\epsilon}{\Delta_-}-\frac{\epsilon(p_-^2-\epsilon^2)}{T^2\Delta_-}\right)-\frac{2y_+}{\Delta_-}\right]\end{aligned}, \tag{A.1}$$

where:

$$T=|\epsilon-\mathbf{p}_-|,\quad Y=\frac{2}{p_-}\ln\frac{\epsilon_+\epsilon_-+p_+p_-+1}{\epsilon},\quad y_+=\frac{1}{p_+}\ln\frac{\epsilon_++p_+}{\epsilon_+-p_+},\quad \delta_+^T=\ln\frac{T+p_+}{T-p_+}, \tag{A.2}$$

where α is the fine-structure constant and r_0 is the classical electron radius. All quantities are measured in the proton rest frame and natural units, normalized to the electron mass. $\epsilon_\pm$, $p_\pm$ are the electron/positron energy and momentum, θ_- is the electron-photon angle, and ϵ is the photon energy.

A.2 Synchrotron radiation in matter: plasma frequency and Razin-Tsytovich effect

The frequency $\omega_{\rm p}$ that enters the parametrization of the synchrotron power is given by:

$$\omega_p \sim \sqrt{\frac{4\pi n_{p,out} e^2}{\gamma_{p,out} m_p} + \frac{4\pi n_{e,out} e^2}{\gamma_{e,out} m_e}}, \tag{A.3}$$

where $n_{p,out}$, $\gamma_{p,out}$, m_p ($n_{e,out}$, $\gamma_{e,out}$, m_e) are the number density, Lorentz factor and mass of the protons (electrons) in the gas [67].

The reason it appears in (2.36) is that the refractive index of the plasma, $n(\omega)$, is affected by fluctuations in its density with characteristic frequency $\omega_{\rm p}$:

$$n(\omega)^2 = 1 - \frac{\omega_{\rm p}^2}{\omega^2}. \tag{A.4}$$

When the refractive index is small, beaming angles become very large, which leads to a suppression of synchrotron emission at the low-frequency end of the emitted spectrum. This phenomenon, which is often referred to as the Razin-Tsytovich effect [68], has been suggested as the cause of a low-frequency cut-off in fast-radio-burst spectra [69].

Figure A.1 shows a comparison between the single-electron synchrotron power spectrum (2.36) in the outflow of AT2019aalc (close to maximum density) and in vacuum. The power spectrum increases at high energies like $\mathcal{P}_{\rm syn} \propto x^{1/3}$ up to a characteristic frequency cut-off:

$$\omega_{\rm c}(\gamma) = \frac{3}{2}\gamma^2 \omega_{\rm B}. \tag{A.5}$$

This behaviour is set by the function $F(x)$, which determines that most of the radiation is emitted at a frequency such that [47].

$$x = x_{\rm max} = 0.29 \sin\theta. \tag{A.6}$$

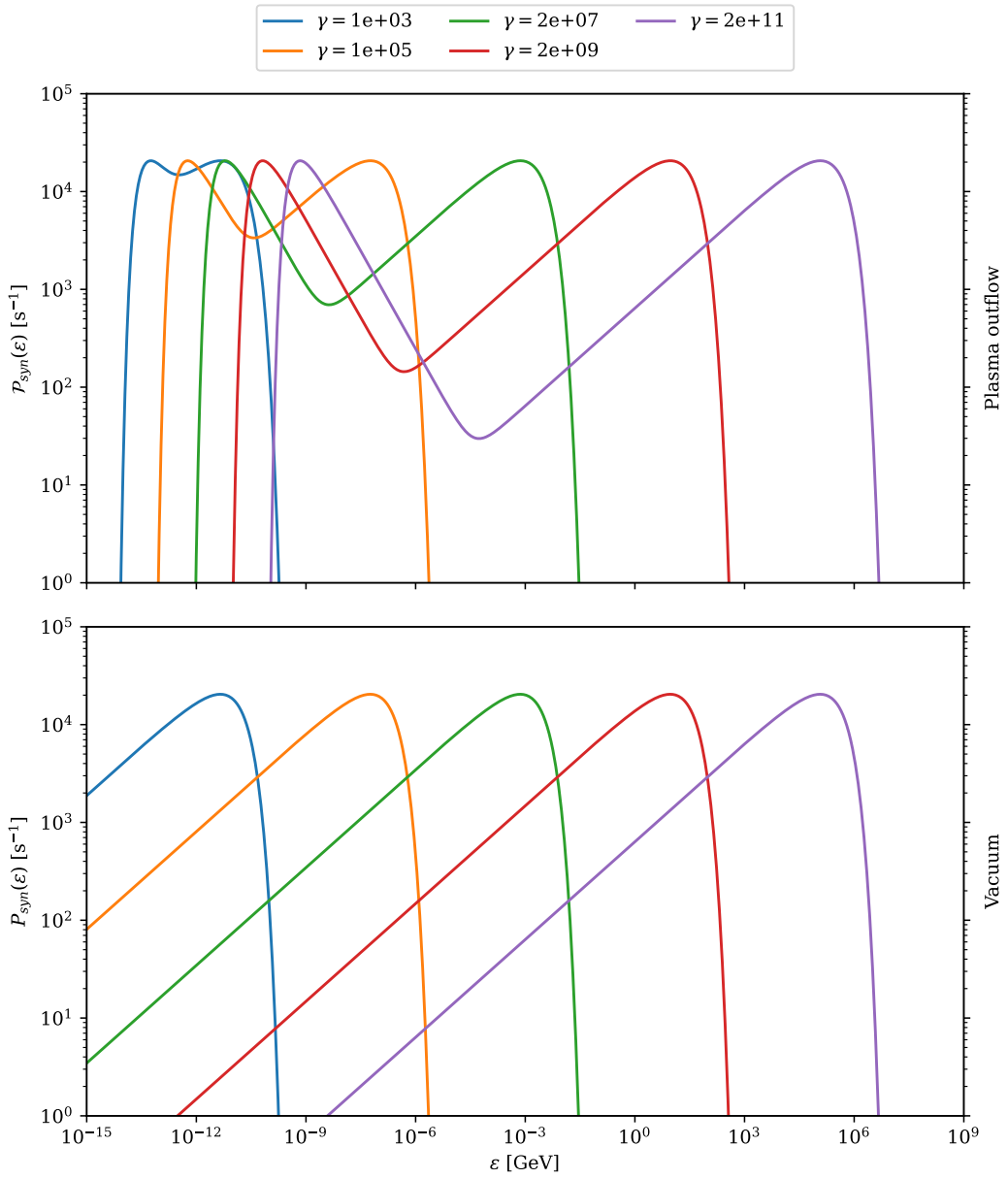

Figure A.1.: Comparison between synchrotron emission in vacuum and in the plasma outflow of TDE AT2019aalc for a viewing angle $\sin\theta \sim 0.6$

The effect of the plasma is that, in addition to ω_c, this equation has another solution at low energies, which is given by the asymptotic behaviour at $\omega \ll \gamma\omega_p$:

$$x \sim \frac{2}{3}\left(\frac{\gamma\omega_p}{\omega}\right)\left(\frac{\omega_p^2\omega_B}{\omega}\right). \tag{A.7}$$

Setting $x = x_{\max}$ in this expression shows that the power spectrum has a resonance at photon energies $\varepsilon = \hbar\omega$:

$$\varepsilon \sim \hbar\omega_{\mathrm{p}} \sqrt{\frac{\gamma}{0.29 \sin\theta} \frac{2\omega_{\mathrm{p}}}{3\omega_{\mathrm{B}}}}. \tag{A.8}$$

Smaller values of ε lead to very high x and thus synchrotron emission in plasma has an additional low-energy cut-off.

B Normalization and time evolution of target backgrounds

B.1 Fiducial parameters

Source	R [cm]	R_d [cm]	B [G]	z	d_L [Mpc]	$M_\bullet$ [$10^7 M_\odot$]	t_dyn [d]
AT2019dsg	5×10^{15}	5×10^{16}	1	0.051	228	0.5	670
AT2019fdr	5×10^{15}	2.5×10^{17}	1	0.267	1369	1.3	1700
AT2019fdr	5×10^{15}	2.0×10^{17}	1	0.036	159	1.6	1970

Table B.1.: Size of the radiation zone (R), dust torus (R_d), magnetic field (B), redshift (z), luminosity distance (d_L), SMBH mass ($M_\bullet$) and dynamical lifetime (t_dyn) of the sources

Source	$\varepsilon_\mathrm{nt}\varepsilon_\mathrm{p}$	ε_out	v_out [c]
AT2019dsg	0.2	0.2	0.1
AT2019fdr	0.2	0.2	0.1
AT2019fdr	0.2	0.2	0.1

Table B.2.: Efficiency in the production of non-thermal protons ($\varepsilon_\mathrm{nt}\varepsilon_\mathrm{p}$), the outflow ($\varepsilon_\mathrm{out}$), and velocity of the outflow (v_out).

The sources are expected to radiate mainly close to the SMBH, where energies are highest, although some dissipation already occurs during circularization. Observations in the OUV bands are thus interpreted as X-rays from the accretion disc, reprocessed by an outer thermal photosphere with radius:

$$R_\mathrm{phot} \sim R_\mathrm{ph0} a_\mathrm{p} \left(\frac{\varepsilon_\mathrm{nt} \dot{M}(t_\mathrm{peak}) c^2}{L_\mathrm{edd}} \right)^l , \tag{B.1}$$

where $\dot{M}(t_{\rm peak})$ is the peak accretion rate, $a_{\rm p}$ is the semi-major axis of the fallback orbit. The proportionality constant $R_{\rm ph0} \sim \mathcal{O}(10^{-3} - 10^{3})$, the conversion efficiency of $\dot{M}$ into non-thermal particles $\varepsilon_{\rm nt} \sim \mathcal{O}(10^{-3} - 10^{-1})$ and the exponent $0.5 < l < 4$ must be fitted from data [53]. For $M_\bullet \sim 10^7 M_\odot$ and a solar-type star, the tidal radius (2.3) is $R_{\rm t} \sim 10^{13}$ cm. Hence, even for quasi-circular orbits $a_{\rm p} \sim R_{\rm t}$, the size of the radiation zone could correspond to $R_{\rm phot}$, although high efficiencies $\varepsilon_{\rm nt} \gtrsim 0.1$ are likely required.

Source	Background	$k_{\rm B}T$ [eV]	L [10^{43} erg s^{-1}]
AT2019dsg	X-ray	72	6.2
	OUV	3.4	28
	IR	0.16	2.8
AT2019fdr	X-ray	56	6.4
	OUV	1.2	140
	IR	0.15	52
AT2019aalc	X-ray	172	0.16
	OUV	0.9	27
	IR	0.16	11

Table B.3.: Temperature and peak luminosity of the photon backgrounds in the radiation zone of the three sources

B.2 Limitations on the analytic study of the fallback rate

As shown by hydrodynamical simulations, $\dot{M}(t) \propto t^{-5/3}$ scaling only holds asymptotically at late times [21]. The Keplerian derivation neglects effects that significantly modify the shape and evolution of $\partial M/\partial\epsilon$ over the lifetime of the system.

Firstly, disruption does not happen instantly. Impulse approximations consider that the star is in hydrostatic equilibrium until it reaches the orbital pericenter $r_{\rm p}$, whereupon it is suddenly destroyed. More realistically, tidal forces will cause the star to inflate before reaching $r_{\rm p}$ [21]. Homologous deformation could still lead to a flat energy distribution, but $\Delta\epsilon$ would be increased compared to the unperturbed case: $\dot{M}(t)$ would evolve faster through lower

values [19]. Regardless, this scenario is not realistic, as the star's response to tidal stresses depends significantly on its inner structure. Denser nuclei may lead to steeper energy distributions, which result in delayed and slower fallbacks compared to the homogeneous case. As an example, $\dot{M}(t)$ has been found to peak earlier and be more narrow for stars with polytropic index $\gamma = 5/3$ than for $\gamma = 4/3$ [33].

These results assume that the unbound stellar material will recede from the SMBH and disperse without affecting the evolution of the back-falling debris. On the contrary, if enough mass is concentrated at the center of the star, its core may remain intact or reform itself after disruption, so circularization will be perturbed by time-dependent interactions with a stellar remnant. In these conditions, Kepler's third Law is not applicable, so $\dot{M}(t)$ is not expected to asymptote to $t^{-5/3}$: instead, analytic calculations show that $\dot{M}(t) \propto t^{-9/4}$ at late times [70]. Deviations from this behaviour can be attributed, at least in part, to the evolution of $\partial M/\partial\epsilon$, which overtime develops a peak around $\epsilon = 0$ due to mass congregation under the remnant's gravity [71].

The strength of this effect and the overall shape of $\dot{M}(t)$ depend on the depth of the tidal encounter, which is measured by the penetration factor $\beta = R_\mathrm{t}/r_\mathrm{p}$. Hydrodynamical simulations find that in grazing events ($0.65 \lesssim \beta$), $\dot{M}$ may fall off faster than $t^{-9/4}$ shortly after the peak, whereas $0.65 < \beta \lesssim 0.85$ may lead to a $\dot{M} \propto t^{-5/3}$ scaling during approximately the same period [34]. Indeed, if the remnant were sufficiently light, its interaction with the stream could be negligible early on, leading to approximately Keplerian orbits [70].

Finally, relativistic effects also influence the evolution of the accretion rate. The importance of post-Newtonian corrections varies with encounter depth: generally, both R_t and r_p are expected to lie far from the event horizon, so the properties of total TDEs occuring near the tidal radius are expected to depend weakly on β [24]. However, classical calculations of the width $\Delta\epsilon$ of the distribution $\partial M_*/\partial|\epsilon_\mathrm{g}|$ may severely underestimate the energy spread in deeply penetrating encounters ($\beta \gtrsim 10$), which has been attributed to shock heating during the vertical compression of the star and to prompt self-intersection of debris streams in the pericenter region [19].

Thus, determining $\dot{M}(t)$ from first principles requires a large number of assumptions on the structure and composition of the star and the geometry

of the system, which are not adequately accounted for in canonical analytic calculations. In a more complete study, it might have been possible to analyse how the expected neutrino fluence varies as a function of these parameters, but given the time constraints in the writing of the thesis, it was considered more productive to fit $\dot{M}(t)$ to the OUV luminosity. This should provide an acceptable approximation of the actual accretion rate over the whole lifetime of the system, at the cost of some insight into the phenomenology of fallback.

C Consistency tests

C.1 Self-consistency of the linear approximation

The transport equation (2.45) used to calculate the cosmic-ray spectra is a linear approximation, which neglects interactions between charged particles and secondary photons. Photon emission by protons occurs mainly in the form of high-energy γ-rays, which are promptly absorbed (Figures 4.9 and 4.10), although reprocessing of this energy via electromagnetic cascades could produce significant luminosity in the form of hard X-rays. Low-energy radiation that could become a scattering target for photomeson production results mainly from the radiative and IC cooling of electrons, as seen in the cooling rates (Figures 4.1 and 4.3) and the time-integrated electromagnetic spectrum (Figure 4.8).

Figure C.1 shows a comparison between the luminosity produced by these processes and the background in the three TDEs. Photomeson production off secondary photons in AT2019dsg and AT2019fdr is inefficient compared to interactions with the background, because their contribution to the target density is subdominant. Hence, corrections to the linear approximation are unlikely to be of order ~ 1.

Interactions with secondary photons in AT2019aalc are expected to be dominated by synchrotron self-Compton emission, i.e. inverse Compton scattering of electrons off their own synchrotron radiation, because this the most efficient cooling mechanism (Figures 4.1 and 4.3). This would lead to an increase in the energy density of γ-rays (Figure 4.8), which could compete with electromagnetic cascades from $\gamma\gamma$ absorption in the OUV background (Figure 4.10). Photomeson production occurs over much longer time scales, so large corrections to the neutrino fluences are not expected. If pion production off X-rays was enhanced, the overall normalization of the pp-neutrino spectrum

would decrease and a peak around $E_\nu \sim 10^6$ GeV in the X-ray neutrino flux could appear.

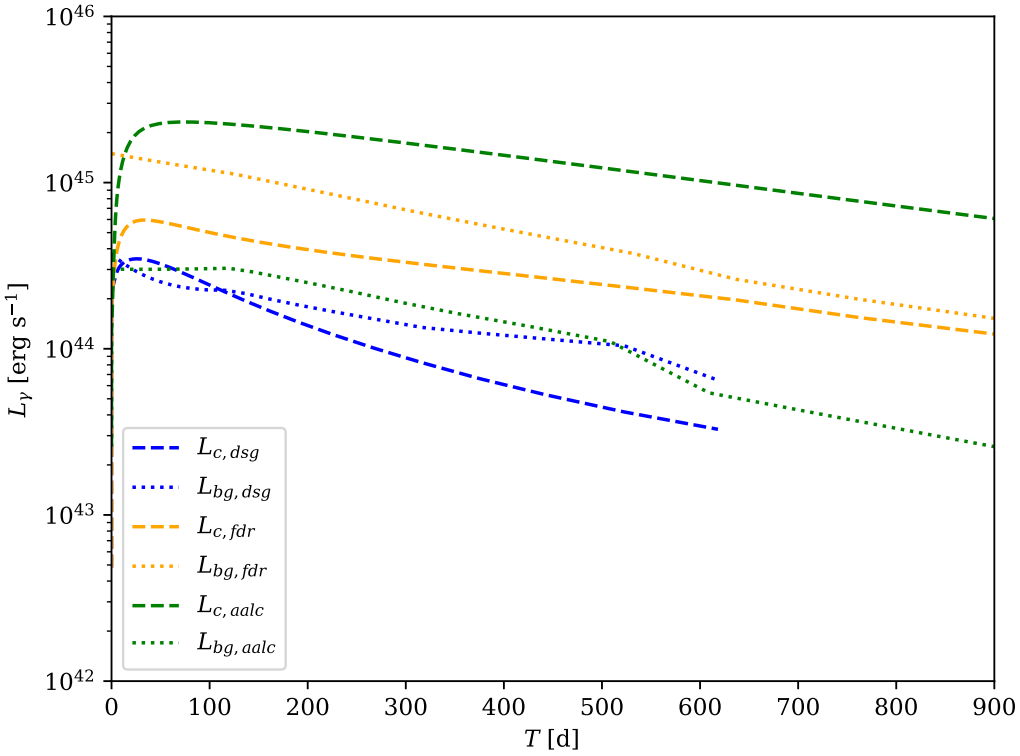

Figure C.1.: Comparison between the background luminosity($L_{\mathrm{bg,i}}$, dotted) and the luminosity of photons from radiative and inverse Compton electron cooling ($L_{\mathrm{c,i}}$) in the TDEs AT2019dsg, AT2019fdr and AT2019aalc.

C.2 Comparison with existing literature

Figure C.2 shows the neutrino fluences obtained with the procedure described in Chapter 3 for a fixed high-energy cut-off $E_{\mathrm{p,max}} = 5 \times 10^6$ GeV and outflow velocity $v_{\mathrm{out}} = 0.5c$. These values correspond to the M-X model in [18], so the results show how the approximations in this work compare with more sophisticated numerical treatments.

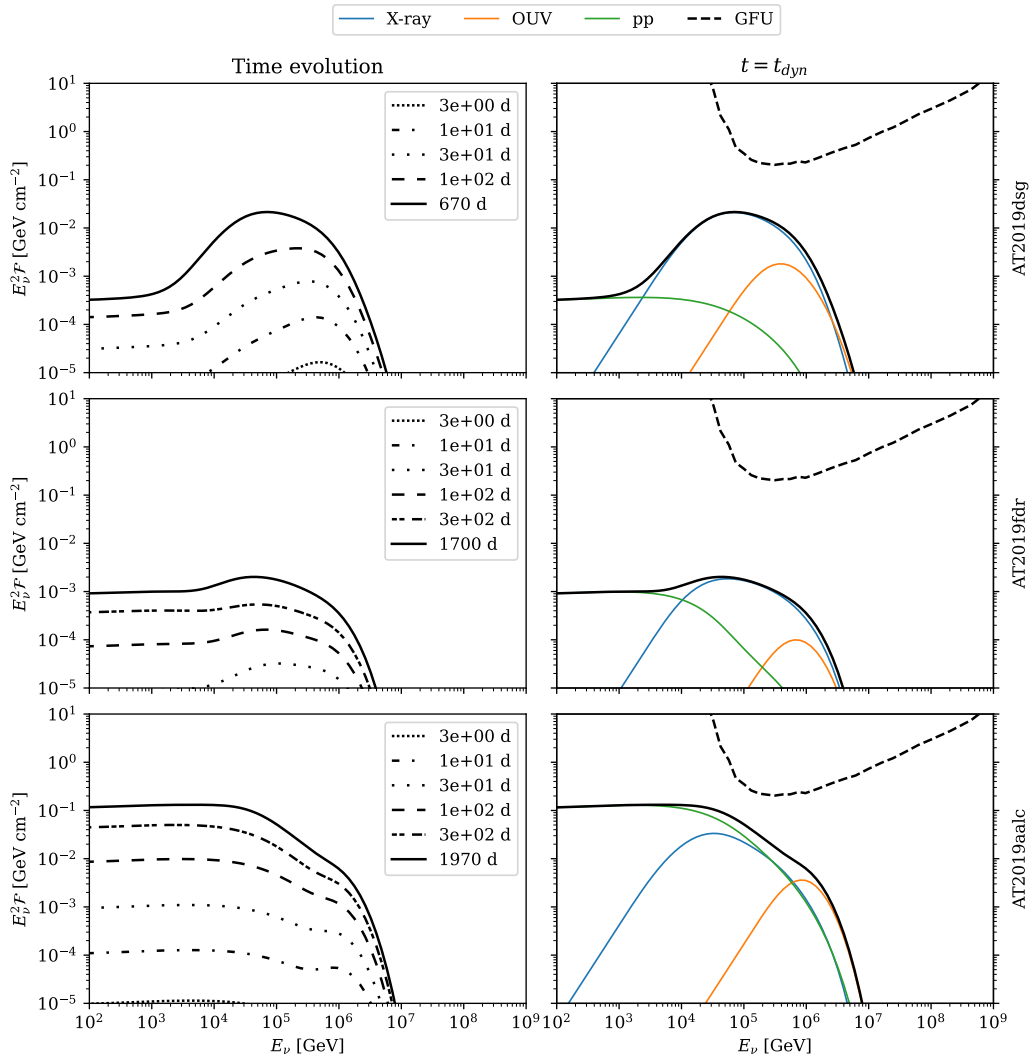

Figure C.2.: Reproduction of the flavour-averaged neutrino fluences in the M-X model of [18] using the same numerical treatment that led to the results in this work.

In all sources, the pp-neutrino fluence matches the spectral distribution and overall normalization in the literature. The X-ray neutrino fluence in AT2019dsg and AT2019fdr is consistent with the results in [18] within a factor ~ 1 in the normalization of the peak. However, the production of OUV neutrinos appears suppressed with respect to the results in said paper. These particles are produced in interactions of protons in the high end of the spectrum, where energy losses in each collision can be significant. This is can be seen from the fact that the photomeson interaction rate (see Figure 3 in [18]) plateaus above $E_\mathrm{p} \gtrsim 10^7$ GeV, whereas the cooling time scale starts decreasing [14]. Hence, it is possible that the continuous cooling

approximation underestimates the amount of proton energy dissipated in the production of neutrinos.

In AT2019aalc, differences in the normalization of the X-ray peak approach a factor ~ 3. It has been checked that this is not due to a missing factor $1/3$ from flavour-averaging. In addition, the spectrum is wider towards lower energies compared to the literature. Since the pp-neutrino fluence is consistent with the published results, it is likely that this results from some unidentified feature at the high-energy end of the proton spectrum. Inefficient photomeson cooling due to low X-ray luminosity might lead to a higher-than-anticipated proton density in the source, which could result in deceitfully high neutrino fluences after folding with the production cross section. Regardless, factors $\mathcal{O}(1)$ are within typical uncertainties in astronomical surveys.

Bibliography

[1] J. Servin and M. Kesden, „Unified treatment of tidal disruption by Schwarzschild black holes“, Physical Review D **95** (2017).

[2] S. Sazonov, M. Gilfanov, P. Medvedev, *et al.*, „First tidal disruption events discovered by SRG/eROSITA: X-ray/optical properties and X-ray luminosity function at $z < 0.6$“, Monthly Notices of the Royal Astronomical Society **508**, 3820–3847 (2021).

[3] E. Hammerstein, S. van Velzen, S. Gezari, *et al.*, „The final season reimagined: 30 tidal disruption events from the ZTF-i survey“, The Astrophysical Journal **942**, 9 (2022).

[4] Y. Cendes, K. D. Alexander, E. Berger, T. Eftekhari, P. K. G. Williams, and R. Chornock, „Radio observations of an ordinary outflow from the tidal disruption event AT2019dsg“, The Astrophysical Journal **919**, 127 (2021).

[5] L. Ferrarese and H. Ford, „Supermassive black holes in galactic nuclei: past, present and future research“, Space Science Reviews **116**, 523–624 (2005).

[6] M. Volonteri, „Formation of supermassive black holes“, The Astronomy and Astrophysics Review **18**, 279–315 (2010).

[7] N. C. Stone and B. D. Metzger, „Rates of stellar tidal disruption as probes of the supermassive black hole mass function“, Monthly Notices of the Royal Astronomical Society **455**, 859–883 (2015).

[8] W. Lu and P. Kumar, „On the missing energy puzzle of tidal disruption events“, The Astrophysical Journal **865**, 128 (2018).

[9] S. van Velzen *et al.*, *Establishing accretion flares from massive black holes as a major source of high-energy neutrinos*, arXiv e-print 2111.09391, 2021.

[10] R. Stein, S. van Velzen, M. Kowalski, *et al.*, „A tidal disruption event coincident with a high-energy neutrino“, Nature Astronomy **5**, 510–518 (2021).

[11]S. Reusch, R. Stein, M. Kowalski, *et al.*, „Candidate tidal disruption event AT2019fdr coincident with a high-energy neutrino“, Physical Review Letters **128**, 10.1103/physrevlett.128.221101 (2022).

[12]M. Ahlers and F. Halzen, „Opening a new window onto the universe with IceCube“, Progress in Particle and Nuclear Physics **102**, 73–88 (2018).

[13]S. R. Kelner, F. A. Aharonian, and V. V. Bugayov, „Energy spectra of gamma rays, electrons, and neutrinos produced at proton-proton interactions in the very high energy regime“, Physical Review D **74**, 034018 (2006).

[14]S. R. Kelner and F. A. Aharonian, „Energy spectra of gamma rays, electrons, and neutrinos produced at interactions of relativistic protons with low energy radiation“, Physical Review D **78**, 10.1103/physrevd.78.034013 (2008).

[15]B. T. Zhang, K. Murase, F. Oikonomou, and Z. Li, „High-energy cosmic ray nuclei from tidal disruption events: Origin, survival, and implications“, Physical Review D **96**, 10.1103/physrevd.96.063007 (2017).

[16]D. Biehl, D. Boncioli, C. Lunardini, and W. Winter, „Tidally disrupted stars as a possible origin of both cosmic rays and neutrinos at the highest energies“, Scientific Reports **8**, 10.1038/s41598-018-29022-4 (2018).

[17]R. Stein (IceCube), „Search for Neutrinos from Populations of Optical Transients“, Proceedings of Science **ICRC2019**, 1016 (2020).

[18]W. Winter and C. Lunardini, „Interpretation of the observed neutrino emission from three tidal disruption events “, The Astrophysical Journal **948**, 42 (2023).

[19]E. Rossi, N. Stone, J. Law-Smith, *et al.*, „The process of tidal disruption by supermassive black holes“, Space Sci Rev **217** (2021).

[20]C. W. Misner, K. S. Thorne, and J. A. Wheeler, *Gravitation* (W. H. Freeman, San Francisco, 1973).

[21]G. Lodato, A. R. King, and J. E. Pringle, „Stellar disruption by a supermassive black hole: is the light curve really proportional to $t^{-5/3}$?“, Monthly Notices of the Royal Astronomical Society **392**, 332–340 (2008).

[22]N. C. Stone, *The tidal disruption of stars by supermassive black holes: an analytic approach*, 1st ed., Springer Theses (Springer Cham, 2015).

[23]T. Alexander, „Stellar dynamics and stellar phenomena near a massive black hole“, Annual Review of Astronomy and Astrophysics **55**, 17–57 (2017).

[24]C. S. Kochanek, „Tidal disruption event demographics“, Monthly Notices of the Royal Astronomical Society **461**, 371–384 (2016).

[25]K. Hayasaki, N. Stone, and A. Loeb, „Circularization of tidally disrupted stars around spinning supermassive black holes“, Monthly Notices of the Royal Astronomical Society **461**, 3760–3780 (2016).

[26]K. Hayasaki and R. Yamazaki, „Neutrino emissions from tidal disruption remnants“, The Astrophysical Journal **886**, 114 (2019).

[27]W. Lu and C. Bonnerot, „Self-intersection of the fallback stream in tidal disruption events“, Monthly Notices of the Royal Astronomical Society **492**, 686–707 (2019).

[28]L. E. Strubbert and E. Quataert, „Optical flares from the tidal disruption of stars by massive black holes“, Monthly Notices of the Royal Astronomical Society **400**, 2070–2084 (2009).

[29]N. Shakura and R. Sunyaev, „Black holes in binary systems. Observational appearance.“, Astronomy and Astrophysics **24**, 337–355 (1973).

[30]I. Kotko and J. Lasota, „The viscosity parameter the properties of accretion disc outbursts in close binaries“, Astronomy and Astrophysics **545**, A115 (2012).

[31]C. Bonnerot, E. M. Rossi, and G. Lodato, „Long-term stream evolution in tidal disruption events“, Monthly Notices of the Royal Astronomical Society **464**, 2816–2830 (2016).

[32]S. A. Balbus and J. F. Hawley, „A powerful local shear instability in weakly magnetized disks. i. linear analysis“, Astroparticle Physics Journal **376**, 214 (1991).

[33]E. C. A. Golightly, C. J. Nixon, and E. R. Coughlin, „On the diversity of fallback rates from tidal disruption events with accurate stellar structure“, The Astrophysical Journal **882**, L26 (2019).

[34]P. R. Miles, E. R. Coughlin, and C. J. Nixon, „Fallback rates from partial tidal disruption events“, The Astrophysical Journal **899**, 36 (2020).

[35]M. Spurio, *Probes of multimessenger astrophysics*, 2nd ed., Astronomy and Astrophysics Library (Springer Cham, 2018).

[36]M. S. Longair, *High energy astrophysics*, 3rd ed. (Cambridge University Press, 2011).

[37]J. H. Matthews, A. R. Bell, and K. M. Blundell, „Particle acceleration in astrophysical jets“, New Astronomy Reviews **89**, 101543 (2020).

[38]A. R. Choudhuri, *The physics of fluids and plasmas: an introduction for astrophysicists* (Cambridge University Press, 1998).

[39]M. Kachelrieß and D. Semikoz, „Cosmic ray models“, Progress in Particle and Nuclear Physics **109**, 103710 (2019).

[40]A. Shalchi, „Diffusive shock acceleration in supernova remnants: On the validity of the Bohm limit“, Astroparticle Physics **31**, 237–242 (2009).

[41]P. Blasi, „The origin of galactic cosmic rays“, The Astronomy and Astrophysics Review **21**, 10.1007/s00159-013-0070-7 (2013).

[42]T. Kamae, N. Karlsson, T. Mizuno, T. Abe, and T. Koi, „Parameterization of γ,e$^{\pm}$ and neutrino spectra produced by $p - p$ interaction in astronomical environments“, The Astrophysical Journal **647**, 692–708 (2006).

[43]R. Workman *et al.* (Particle Data Group), „Review of Particle Physics“, Progress of Theoretical and Experimental Physics **2022**, 083C01, 10.1093/ptep/ptac097 (2022).

[44]L. Morejon, A. Fedynitch, D. Boncioli, D. Biehl, and W. Winter, „Improved photomeson model for interactions of cosmic ray nuclei“, Journal of Cosmology and Astroparticle Physics **2019**, 007 (2019).

[45]G. R. Blumenthal, „Energy loss of high-energy cosmic rays in pair-producing collisions with ambient photons“, Physical Review D **1**, 1596–1602 (1970).

[46]G. B. Rybicki and A. P. Lightman, *Radiative Processes in Astrophysics* (1986).

[47]R. Schlickeiser, *Cosmic ray astrophysics*, Astronomy and Astrophysics Library (Springer Berlin, Heidelberg, 2002).

[48]G. R. Blumenthal and R. J. Gould, „Bremsstrahlung, synchrotron radiation, and compton scattering of high-energy electrons traversing dilute gases“, Rev. Mod. Phys. **42**, 237–270 (1970).

[49]G. Ghisellini, *Radiative processes in high energy astrophysics* (Springer International Publishing, 2013).

[50]L. P. Pitaevskii and E. M. Lifshitz, *Physical kinetics: volume 10 (course of theoretical physics)* (Butterworth-Heinemann, Jan. 1981).

[51]P. Mertsch, „A new analytic solution for 2nd-order fermi acceleration“, Journal of Cosmology and Astroparticle Physics **2011**, 10.1088/1475-7516/2011/12/010 (2011).

[52]D. Wilkins and R. Gallo, „The Comptonization of accretion disc X-ray emission: consequences for X-ray reflection and the geometry of AGN coronae“, Monthly Notices of the Royal Astronomical Society **448**, 703–712 (2015).

[53]B. Mockler, J. Guillochon, and E. Ramirez-Ruiz, „Weighing black holes using tidal disruption events“, The Astrophysical Journal **872**, 151 (2019).

[54]S. Hümmer, M. Rüger, F. Spanier, and W. Winter, „Simplified models for photohadronic interactions in cosmic accelerators“, The Astrophysical Journal **721**, 630–652 (2010).

[55]L. Dai, J. C. McKinney, N. Roth, E. Ramirez-Ruiz, and M. C. Miller, „A unified model for tidal disruption events“, The Astrophysical Journal **859**, L20 (2018).

[56]A. King and S. I. Muldrew, „Black hole winds II: Hyper-Eddington winds and feedback“, Monthly Notices of the Royal Astronomical Society **455**, 1211–1217 (2015).

[57]Y.-F. Jiang, J. M. Stone, and S. W. Davis, „Super-Eddington Accretion Disks around Supermassive Black Holes“, The Astrophysical Journal **880**, 67 (2019).

[58]A. Mücke, J. P. Rachen, R. Engel, R. J. Protheroe, and T. Stanev, „Photohadronic processes in astrophysical environments“, Publications of the Astronomical Society of Australia **16**, 160–166 (1999).

[59]A. Mastichiadis, R. Protheroe, and J. Kirk, „Spectral and temporal signatures of ultrarelativistic protons in compact sources - I. Effects of Bethe-Heitler pair production“, Astronomy and Astrophysics **433**, 765–776 (2005).

[60]E. Peretti, P. Blasi, F. Aharonian, and G. Morlino, „Cosmic ray transport and radiative processes in nuclei of starburst galaxies“, Monthly Notices of the Royal Astronomical Society **487**, 168–180 (2019).

[61]W. H. Press, S. A. Teukolsky, W. T. Vetterling, and B. P. Flannery, *Numerical Recipes in C*, Second (Cambridge University Press, Cambridge, USA, 1992).

[62]S. Koldobskiy, M. Kachelrieß, A. Lskavyan, A. Neronov, S. Ostapchenko, and D. Semikoz, „Energy spectra of secondaries in proton-proton interactions“, Physical Review D **104**, 10.1103/physrevd.104.123027 (2021).

[63]A. Franceschini and G. Rodighiero, „The extragalactic background light revisited and the cosmic photon-photon opacity“, Astronomy and Astrophysics **603**, A34 (2017).

[64]A. Franceschini and G. Rodighiero, „The extragalactic background light revisited and the cosmic photon-photon opacity (corrigendum)“, Astronomy and Astrophysics **614**, C1 (2018).

[65]F. Aharonian, V. Kririllov-Ugriumov, and V. Vardanian, „Formation of Relativistic Electron-Photon Showers in Compact X-Ray Sources“, Astrophysics and Space Science **115**, 201–225 (1985).

[66]E. Blaufuss, T. Kintscher, L. Lu, and C. F. Tung, *The next generation of icecube realtime neutrino alerts*, arXiv e-print, 2019.

[67]A. Sagiv and E. Waxman, „Collective processes in relativistic plasma and their implications for gamma-ray burst afterglows“, The Astrophysical Journal **574**, 861–872 (2002).

[68]A. Crusius and R. Schlickeiser, „Synchrotron radiation in a thermal plasma with large-scale random magnetic fields“, Astronomy and Astrophysics **196**, 327–337 (1988).

[69]V. Ravi and A. Loeb, „Explaining the statistical properties of fast radio bursts with suppressed low-frequency emission“, The Astrophysical Journal **874**, 72 (2019).

[70]E. R. Coughlin and C. J. Nixon, „Partial Stellar Disruption by a Supermassive Black Hole: Is the Light Curve Really Proportional to $t^{-9/4}$?“, The Astrophysical Journal **883**, L17 (2019).

[71]K. Hayasaki, N. Stone, and A. Loeb, „Finite, intense accretion bursts from tidal disruption of stars on bound orbits“, Monthly Notices of the Royal Astronomical Society **434**, 909–924 (2013).